

Constrain the Dark Matter Distribution of Ultra-diffuse Galaxies with Globular-Cluster Mass Segregation: A Case Study with NGC5846-UDG1

JINNING LIANG ^{1,2} FANGZHOU JIANG ^{3,4,*} SHANY DANIELI ⁵ ANDREW BENSON ³ AND PHIL HOPKINS ⁴

¹*School of Physics and Technology, Wuhan University, Wuhan, Hubei 430072, China*

²*WHU-NAOC Joint Center for Astronomy, Wuhan University, Wuhan 430072, China*

³*Carnegie Observatories, 813 Santa Barbara Street, Pasadena, CA 91101, USA*

⁴*TAPIR, California Institute of Technology, Pasadena, CA 91125, USA*

⁵*Department of Astrophysical Sciences, 4 Ivy Lane, Princeton University, Princeton, NJ 08544*

ABSTRACT

The properties of globular clusters (GCs) contain valuable information of their host galaxies and dark-matter halos. In the remarkable example of ultra-diffuse galaxy, NGC5846-UDG1, the GC population exhibits strong radial mass segregation, indicative of dynamical-friction-driven orbital decay, which opens the possibility of using the imaging data alone to constrain the dark-matter content of the galaxy. To explore this possibility, we develop a semi-analytical model of GC evolution, which starts from the initial mass function, the initial structure-mass relation, and the initial spatial distribution of the GC progenitors, and follows the effects of dynamical friction, tidal evolution, and two-body relaxation. Using Markov Chain Monte Carlo, we forward-model the GCs in a NGC5846-UDG1-like potential to match the observed GC mass, size, and spatial distributions, and to constrain the profile of the host halo and the origin of the GCs. We find that, with the assumptions of zero mass segregation when the star clusters were born, NGC5846-UDG1 is well into the dark-matter deficient territory, irrespective of having a cuspy or a cored halo profile, and its GC population has an initial spatial distribution more extended than the smooth stellar distribution. We discuss the results in the context of scaling laws of galaxy-halo connections, and warn against naively using the GC-abundance-halo-mass relation to infer the halo mass of UDGs. We make our model publicly available at <https://github.com/JiangFangzhou/GCevo>.

1. INTRODUCTION

Ultra-diffuse galaxies (UDGs) triggered a frenzy of studies in recent years in the contexts of both understanding the formation of extreme galaxies and testing cosmology (e.g., Sales et al. 2020). Numerical and semi-analytical simulations suggest that UDGs can form via supernovae-driven gas outflows, which transform their hosting dark-matter halos from cuspy to cored together with puffing up their stellar distribution (e.g., Di Cintio et al. 2017; Chan 2019; Jiang et al. 2019), while some UDGs can also populate halos of high specific angular momentum (e.g., Rong et al. 2017; Amorisco & Loeb 2016; Benavides et al. 2022). The formation of UDGs is believed to be facilitated in dense environments, via tidal heating (Jiang et al. 2019; Carleton et al. 2019; Liao et al. 2019) and passive stellar-population dimming (Tremmel et al. 2020). Despite all these theoretical efforts, there are still several aspects of UDGs that remain

intriguing. Notably, UDGs on average have more globular clusters (GCs) than normal galaxies of similar stellar mass (van Dokkum et al. 2016, 2017; Lim et al. 2018). A higher-than-average GC abundance implies that the host dark-matter (DM) halo of the UDG is overly massive for their stellar masses, assuming that UDGs follow the empirical relation between GC abundance and dark-matter halo mass, which is valid over almost five dex of virial mass for normal galaxies (Hudson et al. 2014; Harris et al. 2015, 2017; Burkert & Forbes 2020). In contrast, some UDGs seem to be DM deficient, based on their GC or gas kinematics (van Dokkum et al. 2018, 2019; Guo et al. 2020), which poses a challenge to the standard picture where galaxy formation takes place in DM halos that dominate the mass budget. Hence, to understand the GC populations of UDGs takes center stage in understanding UDG formation in a cosmological context. Notably, the abundance, the spatial distribution, and the kinematics of GCs all contain information of the DM distribution of their hosting UDG.

* Troesh Scholar, fzjiang@caltech.edu, fjiang@carnegiescience.edu

The galaxy NGC5846-UDG1 (UDG1 hereafter) serves as a remarkable example (Müller et al. 2020; Forbes et al. 2021; Danieli et al. 2022b; Bar et al. 2022). On the one hand, it hosts a surprisingly large population of GCs (of ~ 50 within a few stellar effective radii) for its stellar mass of $\sim 10^8 M_\odot$. This translates to an overly massive DM halo of $\sim 10^{11} M_\odot$ assuming the Harris et al. relation (Forbes et al. 2021). On the other hand, the GC population of UDG1 shows a strong radial mass segregation, with more massive GCs lying closer to the center of the galaxy. The mass segregation can be most naturally interpreted as a manifestation of orbital decay caused by dynamical friction (DF), because the strength of DF scales strongly with the perturber mass. And if DF causes the mass segregation, the halo mass should be much lower, because the timescale of orbital decay depends on the perturber-to-host mass ratio (m/M), such that it is shorter than the dynamical timescale of the host galaxy only if $m/M \gtrsim 1/100$ (e.g. Boylan-Kolchin et al. 2008). That is, for a GC of mass $m \sim 10^6 M_\odot$, the host halo cannot be significantly more massive than the stellar mass ($\sim 10^8 M_\odot$) in order to have sufficient orbital decay and mass segregation. Admittedly, this mass-ratio argument was originally made for satellite galaxies entering the host at orbital energies comparable to that of a circular orbit at the virial radius, so the GCs near the host center and thus with much lower orbital energy in principle allow for smaller mass ratios (and therefore larger host halo masses). This, however, requires more detailed modeling that considers the locations of the GCs at birth and the density profile of the host. The strikingly different halo-mass inferences based on the aforementioned two perspectives highlights the importance of such models.

In this work, we first present a semi-analytical model of GC evolution in a composite host potential consisting of stellar and DM distributions. While generally applicable to any low-surface brightness galaxy that exhibits a radial trend of its GC properties, here this model is applied to UDG1 as a proof of concept, showing that the observed mass segregation can be used to constrain the dark-matter halo, together with the other information of the GCs available in the imaging data. As a major improvement over previous studies which also attribute the GC mass segregation in UDG1 to dynamical friction (Bar et al. 2022), a more physical model of the evolution of star clusters under the influence of tidal interactions with the host galaxy and the internal two-body relaxation is considered. Tidal interactions and two-body relaxation drive mass loss and structural changes of the GCs, thus affecting the orbital evolution in a subtle but important way, as we will discuss below. When com-

bined with parameter inference tools, this model enables using imaging data alone, without costly kinematics observations, to statistically constrain the DM distribution of the host galaxy. Additionally, the extreme limit of GC mass segregation is the complete orbital decay of massive GCs to the galaxy center, which is a viable way of forming dense nuclear star clusters as observed in nucleated low-surface-brightness galaxies (Lim et al. 2018; Greco et al. 2018; Sánchez-Janssen et al. 2019; Iodice et al. 2020; Marleau et al. 2021). Our method is therefore also potentially useful in this context.

This work is organized as follows. In Section 2, we introduce our model of GC evolution, and present the workflow of forward modeling the GC population and inferring the host DM profile. In Section 3, we use the observed GC statistics of UDG1 to constrain the model parameters, including the DM halo mass and concentration, as well as the characteristic spatial scale of the initial distribution of the GCs which may shed light upon the origin of the GCs. In Section 4, we compare the model predictions and kinematics observations, discuss the key distinction between a cored halo profile versus a cuspy profile regarding the star cluster population, compare our model to simplistic models that ignore the physics of GC mass and structural evolution, and also comment on potential future developments of this methodology. We draw our conclusions in Section 5.

Throughout, we define the virial radius of the hosting dark-matter halo as the radius within which the average density is $\Delta = 200$ times the critical density for closure, and adopt a flat cosmology with the present-day matter density $\Omega_m = 0.3$, baryonic density $\Omega_b = 0.0465$, dark energy density $\Omega_\Lambda = 0.7$, a power spectrum normalization $\sigma_8 = 0.8$, a power-law spectral index of $n_s = 1$, and a Hubble parameter of $h = 0.7$, unless otherwise mentioned. We use r , R , and l to indicate the three-dimensional galactocentric radius, the projected galactocentric radius, and star-cluster-centric radius, respectively; and denote the mass of a star cluster and that of the host galaxy by m and M , respectively.

2. METHODOLOGY

In this section, we first introduce a dynamical model that describes the evolution of GCs in a composite host potential consisting of dark matter and stars. This model considers the orbital evolution of GCs under the influence of dynamical friction (DF), allowing for the dependence of the strength of DF on the local density profile of the host potential following the recipe of Petts et al. (2015). The GCs evolve in mass and structure in response to the internal two-body relaxation and the

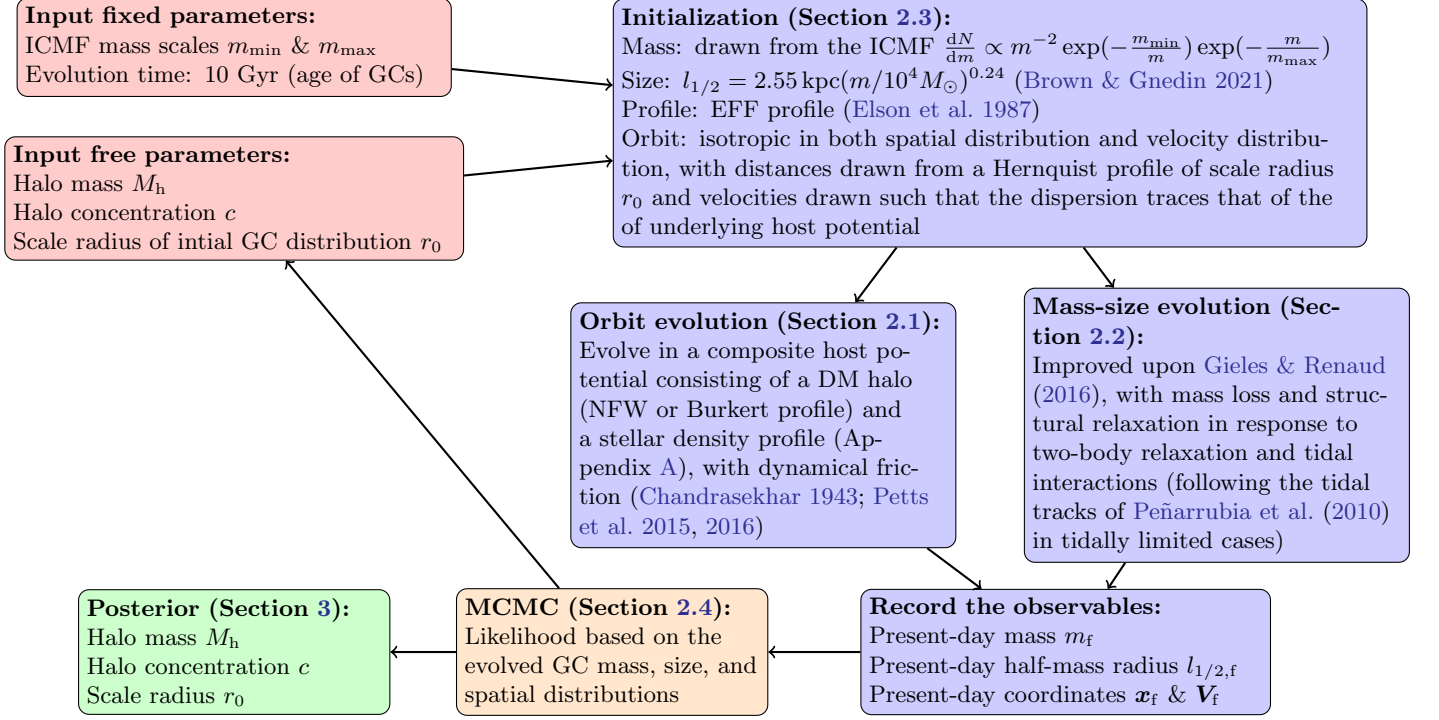


Figure 1. Model workflow.

varying tidal effects along the orbits. We then lay out the model assumptions, including the initial star-cluster mass function, the initial structure of young star clusters, the initial spatial distribution of the star clusters, and the assumptions about the host potential. With these assumptions, the model self-consistently evolves a population of GCs, predicting their evolved mass, size, and spatial distribution, which are then compared to those of the observed GC population. Finally, we combine the model with an MCMC inference tool, to derive constraints on the dark-matter halo of the target galaxy. Figure 1 presents a schematic flowchart that summarizes all the components of our framework, and could be a good starting place for readers who wish to skip the technical details to the results.

2.1. Orbit Evolution: dynamical friction with core-stalling

To follow the orbit of a GC, we solve the equation of motion,

$$\ddot{\mathbf{r}} = -\nabla\Phi + \mathbf{a}_{\text{DF}}, \quad (1)$$

where \mathbf{r} is the position vector, Φ is the gravitational potential, and \mathbf{a}_{DF} is the acceleration due to dynamical friction (DF), given by (Chandrasekhar 1943)

$$\mathbf{a}_{\text{DF}} = -4\pi G^2 m \sum_i \ln \Lambda_i \rho_i(\mathbf{r}) F(< V_i) \frac{\mathbf{V}_i}{V_i^3}. \quad (2)$$

Here, the summation is over different components of the host potential ($i = \text{DM, stars}$), m is the mass of the GC, $\ln \Lambda_i$ is the Coulomb logarithm, \mathbf{V}_i is the relative velocity of the GC with respect to component i , and $F(< V_i)$ is fraction of particles that contribute to DF, which, under the assumption of a Maxwellian distribution, takes form of $F(< V_i) = \text{erf}(X_i) - (2X_i/\sqrt{\pi})e^{-X_i^2}$, where $X_i = V_i/(\sqrt{2}\sigma_i)$, with σ_i the one-dimensional velocity dispersion of component i at position \mathbf{r} .

In the idealized Chandrasekhar picture of dynamical friction, the perturber travels across an infinite homogeneous isotropic medium, and the Coulomb logarithm is defined as $\ln(b_{\text{max}}/b_{\text{min}})$, with b_{max} and b_{min} the maximum and minimum impact parameters, respectively. For perturbers orbiting a galaxy, which is not a uniform medium, the Chandrasekhar DF treatment is used as an approximation, where b_{max} is of the order of the characteristic size of the host system, and b_{min} is the larger of the impact parameter for a 90 degree deflection and the size of the perturber (Binney & Tremaine 2008). In semi-analytical models of satellite-galaxy evolution, it is a common practice to simply assume $\ln \Lambda \sim \ln(M/m)$, where M/m is the mass ratio of the host and the satellite, as the virial radius of a gravitationally bound structure scales with the virial mass (see e.g., Gan et al. 2010, and the references therein). Even constant Coulomb logarithms of $\ln \Lambda \sim 3$ are widely adopted, as major and minor mergers ($M/m \lesssim 10$) contributes to the bulk of

the surviving satellite galaxies. Hence, for the purpose of studying satellite galaxies, where typically the focus is not on the orbital evolution of individual perturbors but on the overall satellite statistics, the simplistic forms of Coulomb logarithm such as $\ln \Lambda \sim \ln(M/m)$ and ~ 3 are reasonable (Green et al. 2021). However, for our purpose here, i.e., to use the GC mass segregation to constrain the dynamical mass distribution, the details of individual orbits are important and thus the simplistic Coulomb logarithms for satellite galaxies may be problematic. For example, $\ln \Lambda \sim \ln(M/m)$ would be very high for GCs and the orbital decay would be unrealistically strong.

Hence, following the more detailed treatment of dynamical friction of Petts et al. (2015), we choose b_{\max} to be

$$b_{\max}(r) = \min \left\{ \frac{r}{\gamma(r)}, r \right\} \quad (3)$$

where $\gamma(r) \equiv -d \ln \rho / d \ln r$ is the local logarithmic density slope of the host potential, and choose b_{\min} as

$$b_{\min} = \max \left\{ l_{1/2}, \frac{Gm}{V^2} \right\}, \quad (4)$$

where $l_{1/2}$ is the half-mass radius of the GC.¹ As such, b_{\max} is a length scale over which the density is approximately constant (Just et al. 2011). To deal with the cases of $b_{\max} \sim b_{\min}$, which can happen when a GC approaches the center of the host, we follow Petts et al. (2016) to substitute the Coulomb logarithm $\ln \Lambda$ in eq. (2) with

$$\frac{1}{2} \ln(\Lambda^2 + 1), \quad \text{where } \Lambda = b_{\max}/b_{\min}. \quad (5)$$

This also empirically accounts for the core-stalling effect (Goerdt et al. 2006; Read et al. 2006; Inoue 2009; Kaur & Sridhar 2018), the phenomenon that the DF acceleration decreases and the orbital decay stalls when the perturber approaches a flat density core, because in the density core, $\gamma(r) \sim 0$, $b_{\max} \sim b_{\min} \sim r$ and $\ln(\Lambda^2 + 1) \sim 0$.

Fig. 2 compares the orbital evolution for different prescriptions of the Coulomb logarithm (as well as for different GC mass evolution models). Focusing on the comparison of the blue and black lines, we can see that the simplistic Coulomb logarithm of $\ln(M/m)$ yields significantly stronger orbital decay than the (more realistic) Petts et al. treatment, which has been well calibrated against numerical simulations.

¹ In practice, we do not distinguish the half-mass radius from the effective radius (i.e., 2D half-light radius), which the observational data for the GCs in UDG1 and the size-mass relation of young star cluster (Brown & Gnedin 2021, as will be discussed in Section 2.3) provide.

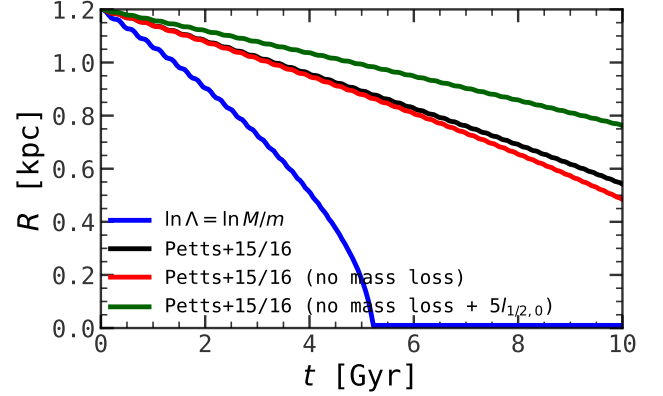


Figure 2. Comparison of orbit evolution for different prescriptions of the Coulomb logarithm in the Chandrasekhar dynamical-friction formula, and for different GC mass evolution model. Here, we release a GC of an initial mass of $m = 10^5 M_\odot$ on a circular orbit of $R = 1.2$ kpc in a host potential consisting of an NFW halo of $M_h = 10^9 M_\odot$ and $c = 10$, and a stellar mass profile of $M_\star = 10^{8.3} M_\odot$ and a scale radius of $r_s = 2$ kpc (which accurately describes the UDG1 stellar mass profile, see Section 2.3). The black line stands for the result using our fiducial model of mass-size evolution (Section 2.2) and the Petts et al. Coulomb logarithm (Section 2.1). The other lines represent the results from varying certain prescriptions, including, using the same fiducial Coulomb logarithm but with no mass loss (red), the same Coulomb logarithm but with no mass loss and with the GC size boosted by a factor of 5 (green), the fiducial mass-size evolution model but with a Coulomb logarithm widely assumed for satellite-galaxy evolution (blue). Note that, first, the mass-size evolution affects orbital evolution via the DF treatment; second, the Petts et al. Coulomb logarithm gives milder orbital decay than the simplistic $\ln \Lambda = \ln M/m$.

2.2. A unified model of mass-size evolution

Globular clusters (GCs) are compact objects that are more resilient to the environmental processes than more diffuse substructures of a galaxy such as DM substructures and gas clouds. This is largely why in previous studies of GC mass segregation, the mass evolution of the GCs was treated simplistically and the structural evolution of the GCs were completely ignored (Bar et al. 2022). However, when dealing with the long-term evolution over the age of the clusters (~ 10 Gyr), the tidal interactions between the GCs and the host galaxy, especially near the center of the host, can result in non-trivial mass and structural change. In the meantime, GCs are internally collisional, and thus lose mass and expand due to the evaporation of stars. This is relevant even in low-density environments. The combination of the external tidal effects and the internal two-body relaxation may result in non-linear mass loss and structural change, which, in turn, affects the orbital evolution, since the

DF acceleration depends on the mass and structure of the perturber, as discussed in Section 2.1. Additionally, the imaging data of the GCs in nearby low-surface-brightness galaxies can be high-resolution enough to provide information about the structure of the GCs. This potentially also contains valuable information of the dynamics besides the mere mass and spatial distribution. For all these reasons, we model the mass-size evolution of the GCs.

Our model of GC mass-size evolution adopts a similar formalism as that of Gieles & Renaud (2016, GR16) but is different in two important aspects. First, GR16 focused on the evolution of newly born star clusters younger than 100 Myr in the vicinity of their birth places, and therefore the dominant tidal effect is the repeated impulsive encounters with giant molecular clouds in the clumpy inter stellar medium surrounding the clusters. Here, we trace the long-term evolution of star clusters over cosmological timescales, and therefore we focus more on the tidal interactions with the background potential. Second, because of the short-term nature, the GR16 model assumes that two-body relaxation causes no mass loss, whereas here we cannot ignore the mass loss from two-body relaxation over the age of the GCs.

We start by differentiating the binding energy $E \propto -Gm^{5/3}\rho_{1/2}^{1/3}$ of a GC, and express the derivative in terms of the mass, m , and the average density within the half-mass radius, $\rho_{1/2}$:

$$\frac{dE}{E} = \frac{5}{3} \frac{dm}{m} + \frac{1}{3} \frac{d\rho_{1/2}}{\rho_{1/2}}. \quad (6)$$

Both tidal interactions and two-body relaxation contribute to the energy increase dE and the mass loss dm , so we distinguish their contributions by denoting dE and dm in two terms with subscripts “t” and “r”, respectively,

$$\frac{dE_t + dE_r}{E} = \frac{5}{3} \frac{dm_t + dm_r}{m} + \frac{1}{3} \frac{d\rho_{1/2}}{\rho_{1/2}}. \quad (7)$$

Following GR16, we introduce a parameter f_t to relate the mass loss to the tidal heating from the interactions with the host potential:

$$\frac{dm_t}{m} = f_t \frac{dE_t}{E}. \quad (8)$$

Similarly, we define an f_r parameter that relates mass loss to the internal heating due to two-body relaxation:

$$\frac{dm_r}{m} = f_r \frac{dE_r}{E}. \quad (9)$$

The values of f_t and f_r can be estimated following analytical arguments or empirical numerical results, as will

be elaborated shortly. It is easier to model the mass losses than to model the energy changes, so we proceed by eliminating the energy terms in eq. (7) using the definitions of f_t and f_r .

The mass loss from tidal stripping is computed as (e.g., Jiang et al. 2019):

$$\frac{dm_t}{m} = -\alpha \xi_t \frac{dt}{\tau_{\text{dyn}}}, \quad (10)$$

where $\xi_t \equiv [m - m(l_t)]/m$ is the fraction of mass outside the tidal radius, with $m(l_t)$ the mass within the instantaneous tidal radius, l_t ; τ_{dyn} is the dynamical time of the host potential at the GC’s instantaneous location, given by

$$\tau_{\text{dyn}} = \sqrt{\frac{3\pi}{16G\bar{\rho}(r)}}, \quad (11)$$

with $\bar{\rho}(r)$ the average density of the host system within radius r ; and $\alpha \approx 0.55$ is an empirical coefficient, calibrated with N -body simulations (Green et al. 2021). The tidal radius is given by (King 1962)

$$l_t = r \left[\frac{m(l_t)/M(r)}{2 - \ln M/\ln r + V_t^2/V_{\text{circ}}^2(r)} \right]^{1/3}, \quad (12)$$

where $M(r)$ is the host mass within radius r , $V_t = |\hat{r} \times \mathbf{V}|$ is the instantaneous tangential velocity, and $V_{\text{circ}}(r)$ is the circular velocity.

Similarly, the evaporation caused by two-body relaxation can be expressed as

$$\frac{dm_r}{m} = -\xi_e \frac{dt}{\tau_r}, \quad (13)$$

where $\xi_e \equiv [m - m(< v_{\text{esc}})]/m$ is the fraction of stars in the tail of the velocity distribution that is larger than the escape velocity, which, for an isolated relaxed GC and thus a Maxwellian velocity distribution, is a constant $\xi_e \approx 0.0074$, and τ_r is a relaxation timescale, given by (Spitzer 1987; Gieles & Renaud 2016)

$$\tau_r \approx 0.142 \text{Gyr} \left(\frac{m}{10^4 M_\odot} \right) \left(\frac{\rho_{1/2}}{10^{11} M_\odot \text{kpc}^{-3}} \right)^{-1/2}. \quad (14)$$

This is the timescale of refilling the high-speed tail of the velocity distribution.

Combining eqs. (7)-(13), we obtain a unified model for GC structural evolution

$$\frac{d\rho_{1/2}}{\rho_{1/2}} = \left[\alpha \left(5 - \frac{3}{f_t} \right) \frac{\xi_t}{\tau_{\text{dyn}}} + \left(5 - \frac{3}{f_r} \right) \frac{\xi_e}{\tau_r} \right] dt. \quad (15)$$

The parameters on the right-hand side of eq. (15) all have analytical estimates or empirical values based on numerical simulations.

GR16 adopted $f_t = 3$ and $f_r = 0$ for the short-term evolution of young star clusters in clumpy interstellar medium, here we estimate f_t and f_r in the context of the long-term evolution of GCs in a gas-less host. To estimate f_t , we consider the limit of negligible two-body relaxation, where the GC evolution can be approximated by the tidal evolution of self-gravitating collisionless systems, which has been extensively studied and documented in the context of DM subhalos (e.g., Peñarrubia et al. 2010; Benson & Du 2022). Peñarrubia et al. (2010) calibrated the tidal evolutionary tracks for DM subhalos using N -body simulations in terms of the maximum circular velocity v_{\max} and the corresponding radius l_{\max} as functions of the bound mass fraction $x = m(t)/m(0)$ and the inner logarithmic density slope $s = -d \ln \rho / d \ln l|_{l \rightarrow 0}$. Turning off two-body relaxation by setting the second term of eq. (15) to zero, i.e.,

$$\frac{d\rho_{1/2}}{\rho_{1/2}} = \alpha \left(5 - \frac{3}{f_t} \right) \xi_t \frac{dt}{\tau_{\text{dyn}}}, \quad (16)$$

we can therefore find f_t by matching the structural evolution according to eq. (16) in terms of v_{\max} and l_{\max} to the tidal track of Peñarrubia et al. (2010) for the case of $s = 0$, since star clusters are generally well described by the Elson et al. (1987) profile and have flat density cores (see Section 2.3). We find that f_t is of order unity and mildly decreases with the bound mass fraction:

$$f_t = 0.77x^{0.19}, \quad x = m/m(0). \quad (17)$$

To estimate f_r , we follow Gieles et al. (2011) and the seminal work of Hénon (1965) to express the energy change of an isolated GC due to two-body relaxation as

$$\frac{dE_r}{E} = -\zeta \frac{dt}{\tau_r}, \quad (18)$$

where $\zeta \approx 0.0926$, assuming equal stellar masses of $0.5M_\odot$ and a Coulomb logarithm of 10 within the star cluster.² Comparing eqs. (9), (13), and (18), we obtain

$$f_r = \xi_e / \zeta \approx 0.08. \quad (19)$$

In summary, for each timestep along the orbit, we evolve the mass of a GC using eqs. (10) and (13), and update the structure of the GC using eq. (15), with the parameters $\alpha = 0.55$, $f_r = 0.08$, and f_t given by eq. (17). The initial mass and structure of a GC is chosen according to the assumptions that we will present in Section 2.3.

² For any realistic stellar mass spectrum, the ζ parameter is larger, up to ~ 0.5 as discussed in GR16.

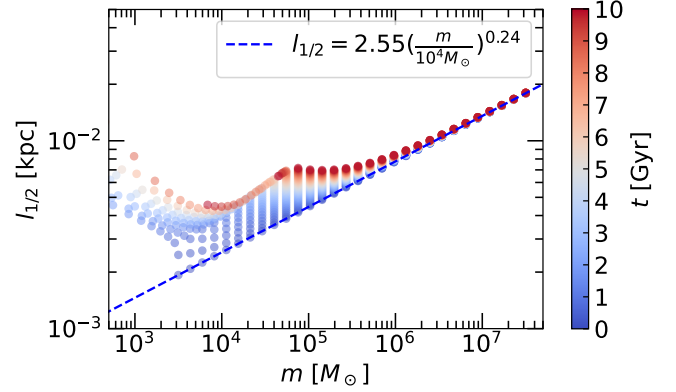


Figure 3. Illustration of the mass-size evolution of star clusters over 10 Gyr according to the model presented in Section 2.2. The star clusters are initialized with masses uniform in $\log m$, sizes following the observed size-mass relation of young star clusters (Brown & Gnedin 2021, blue dashed line), and circular orbits of $r = 5$ kpc in a host potential consisting of an NFW halo with $M_h = 10^{12} M_\odot$ and $c = 10$ and a UDG1-like stellar profile. The evolution is mass-dependent, with massive clusters almost intact and low-mass clusters expanding first and then quickly getting tidally truncated and disrupted.

Fig. 3 illustrates the behavior of GCs in the size-mass plane over 10 Gyr according to this model. The GCs are initialized with masses uniformly distributed in logarithmic mass and with sizes according to the median observed size-mass relation of young star clusters (Brown & Gnedin 2021, as will be discussed in Section 2.3). Clearly, the evolution depends on the initial mass. For the most massive GCs ($m \gtrsim 10^6 M_\odot$), the size and mass barely evolve. For intermediate mass GCs ($m \approx 10^{4.5-6} M_\odot$), the main effect is expansion due to two-body relaxation, while the mass evolution is marginal. Basically, within 10 Gyr, the expansion barely makes their mass distribution extend to the tidal radius, so there is almost no tidal truncation. For lower mass clusters ($m \lesssim 10^4 M_\odot$), tidal truncation quickly takes effect as they expand, so they start to lose mass quickly and even dissolve. These mass-dependent behaviors work together to shape the evolved GC mass function in qualitatively the correct direction to that observed, peaking at $m \sim 10^5 M_\odot$. The evolved GC mass distribution would be insensitive to the low-mass end of the initial cluster mass function. With low mass GCs stripped and dissolved, intermediate mass GCs experiencing weak DF, and massive GCs largely intact and thus always experiencing the strongest DF, mass segregation would naturally arise.

2.3. Model assumptions and GC initialization

We emphasize that the scenario that this study focuses on is that the observed GC mass-segregation signal is driven by DF and that the strength of it can be used to constrain the DM distribution the host galaxy. Hence, the assumptions are chosen to keep the setup simple and to serve the purpose of testing the constraining power of GC mass segregation on DM halo properties. We assume that the initial cluster mass function (ICMF) follows a power-law with exponential truncations at both the high-mass and low-mass ends (Trujillo-Gomez et al. 2019):

$$\frac{dN}{dm} \propto m^\beta \exp\left(-\frac{m_{\min}}{m}\right) \exp\left(-\frac{m}{m_{\max}}\right), \quad (20)$$

where $\beta = -2$ reflects hierarchical molecular cloud formation, and m_{\min} and m_{\max} are the lower and upper characteristic scales. We keep $m_{\min} = 10^{5.5} M_\odot$ and $m_{\max} = 10^8 M_\odot$ fixed for simplicity, after having verified that the results are not sensitive to the detailed values as long as they allow for the existence of GCs covering the mass range of $\sim 10^{4.5}$ to $10^6 M_\odot$ ³. This is partly due to the mass-dependent evolution as shown in Fig. 3, that the low-mass clusters will dissolve in the end.

We describe the density profile of a star cluster by an Elson et al. (1987, EFF) functional form,

$$\rho(l) = \frac{\rho_0}{(1 + l^2/a^2)^\eta}, \quad (21)$$

where $\rho_0 = \Gamma(\eta)m/[\pi^{3/2}\Gamma(\eta-1)a^3]$ is the central density, with $\Gamma(x)$ the Gamma function, m the mass of the cluster, -2η the outer logarithmic slope of the density profile, and a a scale radius linked to the half-mass radius by

$$a = l_{1/2}/(2^{2/\eta-3} - 1)^{1/2}. \quad (22)$$

We adopt $\eta = 2$ such that the outer density slope is -4 , which is motivated by observations of the light profile of young star clusters (Ryon et al. 2015), and assume that it is fixed across evolution such that the density-profile evolution is manifested only by the mass and size evolution as in Section 2.2. More analytical properties of the EFF profile can be seen in Appendix B.

³ We emphasize that m_{\min} shall not be regarded as the minimum initial GC mass: because of the functional form of eq. (20) and the power-law slope of $\beta = -2$, with $m_{\min} = 10^{5.5} M_\odot$, the minimum initial star-cluster mass can reach $\sim 10^4 M_\odot$. Similarly, m_{\max} is not the maximum GC mass. Practically, the initial GC masses drawn from eq. (20) with the aforementioned parameter choices peaks at $10^{5.3} M_\odot$ and extends to $\sim 10^{4.5} M_\odot$ and $10^{6.2} M_\odot$ at the tails.

With the initial mass drawn from the ICMF, we determine the initial size by sampling from a log-normal distribution based on the observed size-mass relation for young star clusters in the Legacy Extragalactic UV Survey (Brown & Gnedin 2021): the median half-mass radius is given by

$$l_{1/2} = 2.55 \text{ kpc} \left(\frac{m}{10^4 M_\odot} \right)^{0.24}, \quad (23)$$

and the 1σ scatter at fixed mass is approximately 0.25 dex.

We assume that the GC progenitors were all born 10 Gyr ago (Müller et al. 2020; Bar et al. 2022) and that they were isotropically distributed following a Hernquist (1990) profile ($\rho(r) \propto 1/[r(r+r_0)^3]$) with no mass segregation at birth. The initial spatial scale, r_0 , of the GC-progenitor spatial distribution is a free parameter to be constrained. We ignore GC-GC encounters and mergers everywhere, after verifying that the merger rate is approximately 0.03 Gyr^{-1} per GC assuming ~ 100 GCs in a dwarf halo of $10^{10} M_\odot$, using the merger criterion in Dutta Chowdhury et al. (2020). The only exception is for the galaxy center, where there can be GCs that have lost their orbital angular momenta completely before getting dissolved and merge to form a nuclear star cluster (see Section 4.2).

We treat the host system as a combination of a smooth stellar-mass distribution and a DM halo, both of which remain constant during the GC evolution. For the stellar profile, to facilitate orbit integration, we fit a density profile with simple analytical expressions of the gravitational potential to the observed stellar density profile⁴, given by

$$\rho(r) = \frac{\rho_{0,*}}{(1+x)(1+x^3)} \quad (24)$$

where $x = r/r_s$, and $\rho_{0,*} = 27M_*/[4\pi(9+2\sqrt{3}\pi)r_s^3]$ with $M_* = 10^{8.3} M_\odot$ and $r_s = 2 \text{ kpc}$ (see Appendix A.3 for more details).

For the DM halo of UDG1, we consider two functional forms, representing cuspy and cored halos, respectively – first, the NFW (Navarro et al. 1997) profile,

$$\rho(r) = \frac{\rho_0}{x(1+x)^2}, \quad (25)$$

where $x = cr/r_{\text{vir}}$, and $\rho_0 = c^3 \Delta \rho_{\text{crit}}/[3f(c)]$ with $f(x) = \ln(1+x) - x/(1+x)$; second, the Burkert (1995)

⁴ Bar et al. (2022) adopted a mass-to-light ratio from Müller et al. (2020) and derived a 3D stellar density profile from the 2D Sersic profile that best fit the surface brightness –see Figure 4 of Bar et al. (2022).

profile,

$$\rho(r) = \frac{\rho_0}{(1+x)(1+x^2)}, \quad (26)$$

where $x = cr/r_{\text{vir}}$, and $\rho_0 = M_h / [2\pi r_{\text{vir}}^3 g(c)c^3]$ with $g(x) = 0.5 \ln(1+x^2) + \ln(1+x) - \arctan x$. It is not obvious whether a core or a cusp is more advantageous for producing the GC mass segregation: for a cored profile, GCs would pile up where the density slope turns flat due to the core-stalling effect, so that massive and low-mass GCs are mixed; for a cuspy profile, DF could be so strong that massive GCs sink completely to the center, but leaving the outer GCs not very different in mass. It is interesting to explore which case produces mass segregation more easily and what other differences they may cause. We initialize the velocities of the GCs such that they are isotropically distributed and trace the velocity dispersion of the composite host potential.

2.4. Parameter Inference

We use the affine invariant Markov chain Monte Carlo (MCMC) ensemble sampler, **emcee** (Foreman-Mackey et al. 2013), to constrain the properties of the host DM halo (i.e. the halo mass M_h and the halo concentration parameter c) and the initial scale length of the GC distribution r_0 using the observed GC statistics. The observational data that provide the constraints involves the present-day masses of the GCs (m), the half-mass radii ($l_{1/2}$), and the projected distances to the galaxy center (R), from Danieli et al. (2022b). With the primary focus being the segregation in mass, we adopt three logarithmic mass bins (as indicated in Fig. 5), and use the median quantities $\langle \log m \rangle_i$, $\langle l_{1/2} \rangle_i$, and $\langle \log R \rangle_i$ for constructing the likelihood. We parameterize the radial mass segregation using two set of quantities: the slopes $\gamma_{ij} \equiv (\langle \log m \rangle_j - \langle \log m \rangle_i) / (\langle \log R \rangle_j - \langle \log R \rangle_i)$, and the number of GCs at each bin relative to the total number of the surviving GCs, f_i . These two quantities measure the steepness of the radial mass segregation and sample the evolved GC mass function, respectively. Overall, we consider a logarithmic likelihood given by

$$\ln(p) = -\frac{1}{2} \sum_k w_k \frac{(y_{k,\text{data}} - y_{k,\text{model}})^2}{y_{k,\text{data}}^2}, \quad (27)$$

where $y_{k,\text{data}}$ and $y_{k,\text{model}}$ refer to the observed values and model predictions, respectively, and y_k represents one of the following quantities, $\{\langle \log m \rangle_i\}$, $\{\langle \log R \rangle_i\}$, $\{\langle l_{1/2} \rangle_i\}$, $\{\langle \gamma_{ij} \rangle_{j>i}\}$, and $\{f_i\}$, with $i, j = 1, 2, 3$, and w_k is the weight for k th quantity. We adopt uniform weighting ($w_k = 1$), which essentially gives the mass-segregation signal an emphasis because there are three quantities that measure it. We adopt uniform priors

for the parameters of interest, i.e., the halo mass M_h , the halo concentration c , and the initial spatial scale r_0 , within ranges that can be chosen according to the galaxy of interest (see Section 3 for example).

To speed up the MCMC inference, instead of evolving the GC populations on the fly for different parameter combinations in each random-walk iteration, we pre-compute the model predictions $y_{k,\text{model}}$ on a mesh grid spanned by the parameters of interest, recording the values of on this mesh grid. During the MCMC random walk, $y_{k,\text{model}}$ is evaluated by linear interpolation. Details about the interpolation method and examples of the pre-computed model predictions can be seen in Appendix C. Note that we opt for not including the total number of GCs as a quantity of interest in our model. This allows us to focus more efficiently on the correlations and on the moments of the observables. Hence, when pre-computing the models, we adopt arbitrarily large initial number of GCs to ensure smooth interpolations. When presenting the model realizations corresponding to the posterior models, we adopt an initial GC number that leads to a surviving GC abundance comparable to the observed one.

3. THE DARK-MATTER HALO OF NGC5846-UDG1

As a proof-of-concept, we apply the aforementioned method to study the galaxy NGC5846-UDG1 and its GC population. Recall that the free parameters to be constrained are the halo mass M_h , the halo concentration c , and the scale radius r_0 of the Hernquist profile from which the initial locations of the star clusters are drawn. We assume uniform priors of $\log(M_h/M_\odot) \in [8, 10.5]$, $c \in [2, 15]$, and $r_0 \in [0.1, 5]$ kpc. We limit the initial star clusters between 0.1 and 5 kpc, choose $M_{\text{min}} = 10^{5.5} M_\odot$ and $M_{\text{max}} = 10^8 M_\odot$ for the ICMF, and evolve the GCs for 10 Gyr, after verifying that the results are not sensitive to slight variations of these values. For the MCMC, we use 64 random walkers, and show results of 15000 iterations after 300 burn-in timesteps. Below, we first present the posterior distributions of the model parameters and compare the model predictions with the data, for the two halo-profile assumptions respectively, and then discuss the results in the context of scaling relations of galaxy-halo connection.

3.1. NFW halo

Fig. 4 shows the posterior distributions for NFW host halos. The mode values (in the 3D parameter space) are $M_h = 10^{8.66} M_\odot$, $c = 5.24$, and $r_0 = 4.05$ kpc, as indicated by the red stars. The median values, together with the 16th and 84th percentiles, are $\log M_h = 8.53^{+0.49}_{-0.37} M_\odot$, $c = 6.97^{+4.88}_{-2.99}$, and $r_0 = 3.11^{+1.30}_{-1.50}$ kpc, as

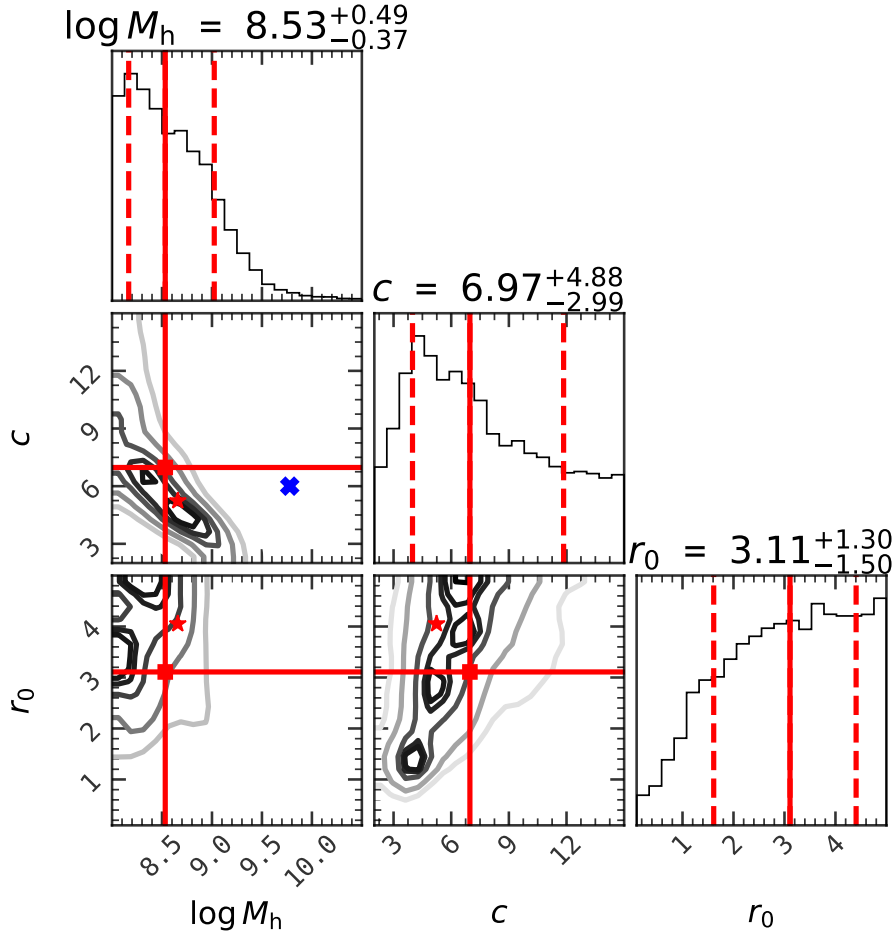


Figure 4. Posterior distributions of the model parameters (halo mass M_h , halo concentration c , and the scale radius r_0 for the initial star-cluster distribution), assuming an NFW host halo. The red lines indicate the median and the 16th and 84th percentiles. The red stars indicate the 2D projections of the 3D mode value. The blue cross in the c - $\log M_h$ plane stands for the halo parameters as adopted in Bar et al. (2022) Figure 5 (see Section 4.3).

indicated by the red lines. We generate a model realization with the mode-value parameters, and compare it with the data, as shown in Fig. 5.

First, focusing on the R - m plane, there is a clear trend of mass segregation in the model realization, very similar to that observed. The parameter space that can give rise to such a prominent mass segregation is actually rather limited: a halo significantly more massive than $10^9 M_\odot$ can hardly reproduce the slope and the small distances of the most massive GCs, no matter how we vary the halo concentration c or the initial spatial scale r_0 . In Appendix C, for example, we show the median R - m relations for different halo masses and with different r_0 .

Second, the evolved GC size distribution and the size-mass relation are reproduced fairly well: note that the initial GC size distribution is quite broad, but the evolution shrinks the size distribution significantly to better match that observed. Related, the evolved GC size-mass

relation is almost flat, as observed, while the initial one has a slope of 0.24. This is largely because the low-mass GCs expand due to two-body relaxation and tidal interactions over the long-term evolution whereas the massive ones are almost intact, as illustrated in Fig. 3.

Third, the GC mass function evolves from an initial broad distribution towards a narrower distribution in better agreement with what is observed. This is partly because of the depletion of the lowest-mass clusters ($m \lesssim 10^{4.5} M_\odot$), but also partly because some of the most massive clusters ($m \gtrsim 10^6 M_\odot$) have sunk to the center of the system to contribute to the formation of a nuclear star cluster and thus not taken into account in the GC mass function shown here. We will discuss this further in Section 4.

As can be seen from the posterior distribution shown in Fig. 4, there is an anti-correlation between halo concentration c and halo mass M_h . This trend is largely driven by the mass segregation, which can only be

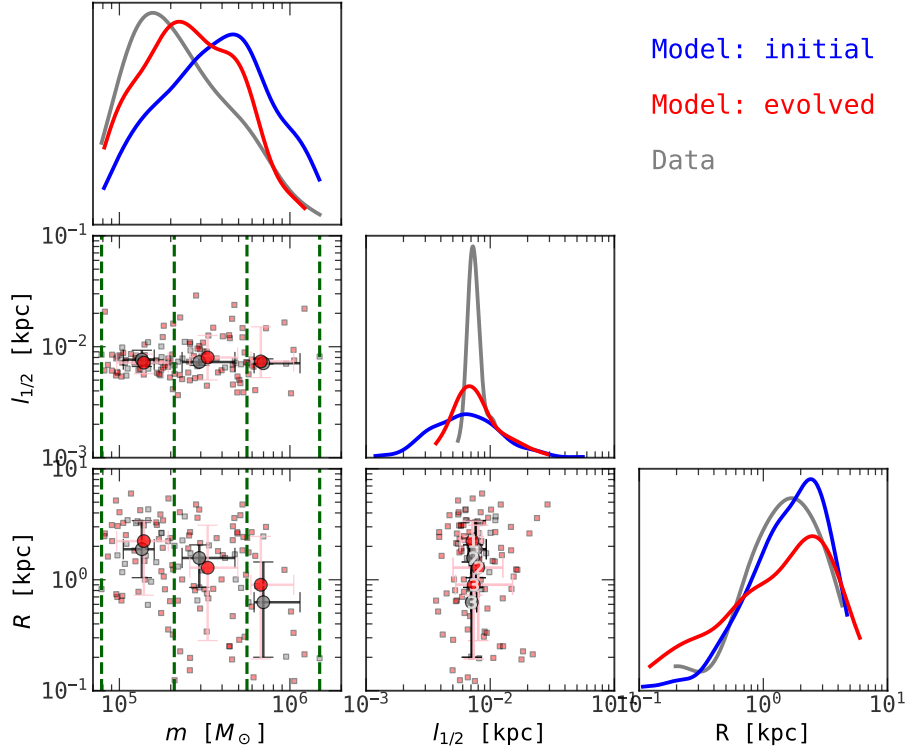


Figure 5. Model realization with an NFW halo and the mode parameters ($M_h = 10^{8.66} M_\odot$, $c = 5.24$, $r_0 = 4.05$ kpc) compared to the data. The diagonal panels show the one-point functions of star-cluster mass m , size $l_{1/2}$, and galactocentric distance R . The other panels show the 2D distributions. The red circles stand for the median model predictions in the three mass bins (whose boundaries are indicated by the vertical dashed green lines), while the gray circles are those from observation. The error bars indicate the 16th and 84th percentiles. The numbers i shown in the center of the circles in the $R - l_{1/2}$ plane means that this point is for the i th mass bin.

achieved with an appropriate amount of DF – overly strong DF would result in orbital decay that is too fast, such that massive GCs sink to the center, forming a stellar nucleus instead of contributing to a continuous radial mass gradient; overly weak DF would have no effect. The strength of DF at a radius r can be measured by the quantity $r\rho(r)/M(r)$, as can be seen from eq. (2), where the DF acceleration a_{DF} scales linearly with the local density $\rho(r)$ and inversely with the velocity squared, $V^2 \sim GM(r)/r$. For NFW profiles, it is easy to show that this quantity increases with increasing halo mass or decreasing concentration, for the radius range of interest ($R \lesssim 5$ kpc). This is not the case for a Burkert profile, as will be discussed shortly in Section 3.2.

Given a stellar mass of $M_\star \sim 10^8 M_\odot$, the galaxy is DM deficient, despite the degeneracy between c and M_h . At the mode values, the halo mass of $M_h = 10^{8.66} M_\odot$ corresponds to a high M_\star - M_h ratio of ~ 0.2 . Even for extremely low concentrations of $c \sim 3$, the halo mass will not get significantly higher than $10^{9.5} M_\odot$, i.e., $M_\star/M_h \sim 0.03$, still much higher than that of normal dwarf galaxies. Also interestingly, the concentration is

much lower than the cosmological average values. For a halo mass of $M_h \sim 10^9 M_\odot$, the expected halo concentration is ~ 25 (Dutton & Macciò 2014), $\sim 3\sigma$ higher than the median of the posterior. We will discuss the implications of these findings in Section 3.3.

There is a positive correlation between the halo concentration c and the characteristic distance r_0 of the initial GC distribution. Similarly, this can also be attributed to the mass segregation – star-clusters that start with a larger r_0 require stronger DF to decay to the current distances, and a stronger DF acceleration is achieved by a higher concentration and thus a higher density.

Despite the r_0 - c correlation, the initial star-cluster distribution is more extended than the present-day smooth stellar distribution of UDG1 – even at the lower end of the ridge-line of the r_0 - c posterior, we have $r_0 \sim 1$ kpc, corresponding to an effective radius of ~ 2.4 kpc, larger than the effective radius of the smooth stellar mass (2 kpc). This may shed light upon the formation mechanisms. First, the star clusters may have formed *ex situ* and been brought in by satellite galaxies, which have since then been disrupted in UDG1 and released their

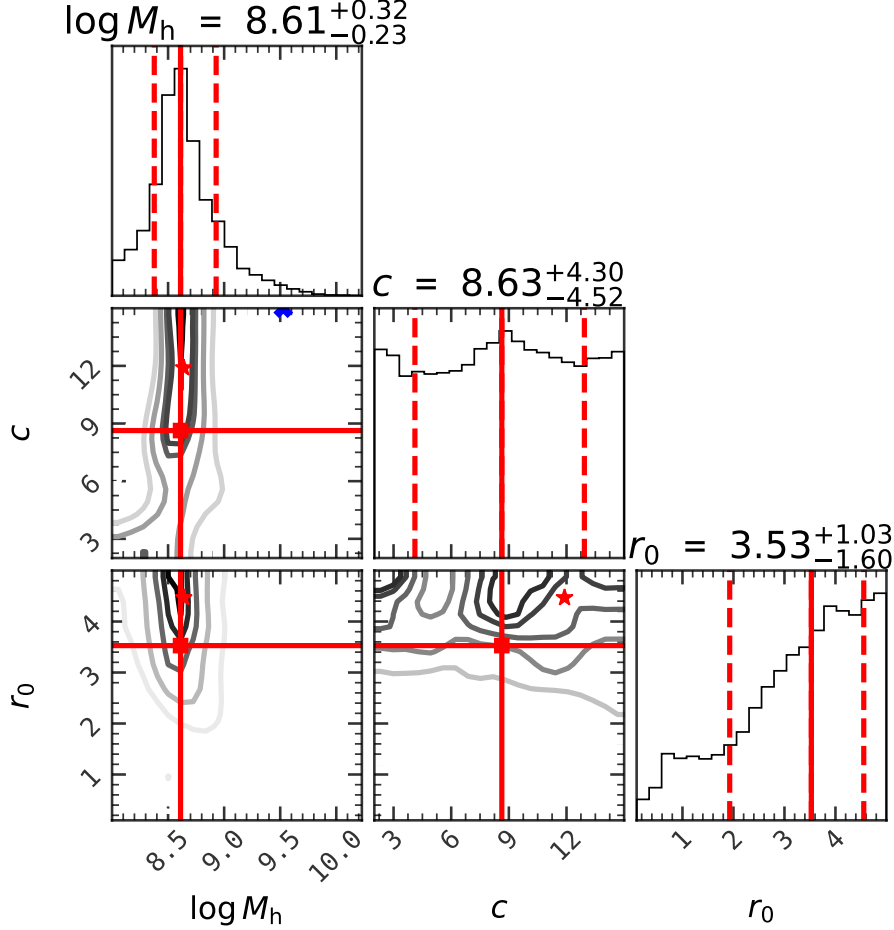


Figure 6. The same as Fig. 4, but assuming a Burkert host halo.

star clusters. Second, the star clusters may have formed *in situ* but in an extended configuration or with high velocity dispersion, e.g., during collisions of high-redshift gas clouds that belongs to different satellite galaxies (Silk 2017; van Dokkum et al. 2022).

3.2. Burkert halo

Fig. 6 shows the posterior distributions with a Burkert halo. The results are overall similar to those with an NFW halo, but with subtle, interesting differences. The mode values are $M_h = 10^{8.64} M_\odot$, $c = 11.90$, and $r_0 = 4.47$ kpc, and the medians with the 16th and 84th percentiles are $\log(M_h/M_\odot) = 8.61^{+0.32}_{-0.23} M_\odot$, $c = 8.63^{+4.30}_{-4.52}$, and $r_0 = 3.53^{+1.03}_{-1.60}$ kpc. The halo mass is slightly higher than that of the NFW case, but still leaves the galaxy in the DM deficient territory. The concentration is significantly higher than the NFW case, but still smaller than the cosmological average expected for halos of the mode/median mass.

For the Burkert halo, the degeneracy between concentration and halo mass is absent. Again, we can understand this using the proxy of the strength of DF,

$\rho(r)/V_{\text{circ}}(r)^2$ – while in the NFW case, decreasing c and increasing M_h can both increase this quantity for the radius range of interest ($r \lesssim 5$ kpc), it is no longer the case with a Burkert profile. Instead, the $\rho(r)$ change when varying c almost exactly cancels that in V_{circ}^2 . This is also why the constraining power on halo concentration is rather weak, and there is no obvious correlation between c and the initial scale distance r_0 . For the initial scale distance r_0 , we also obtain a mode/median value that is larger than the effective radius of UDG1, so the same formation scenarios could be hypothesized.

Similarly, we generate a model realization of the GC population with the mode parameter values of the Burkert halo, and as shown in Fig. 7, it also reproduces most aspects of the data. Hence, either a cuspy halo or a cored halo can reproduce the average trend of mass segregation. However, there is a noticeable difference, that the GCs can reach smaller distances in a Burkert halo. In the R - m plane, very few model GCs with $m \sim 10^5 M_\odot$ populate the region of $R \lesssim 1$ kpc in the NFW case, but here there is a more significant low- R tail. The same trend was actually also seen in Bar et al. (2022), which

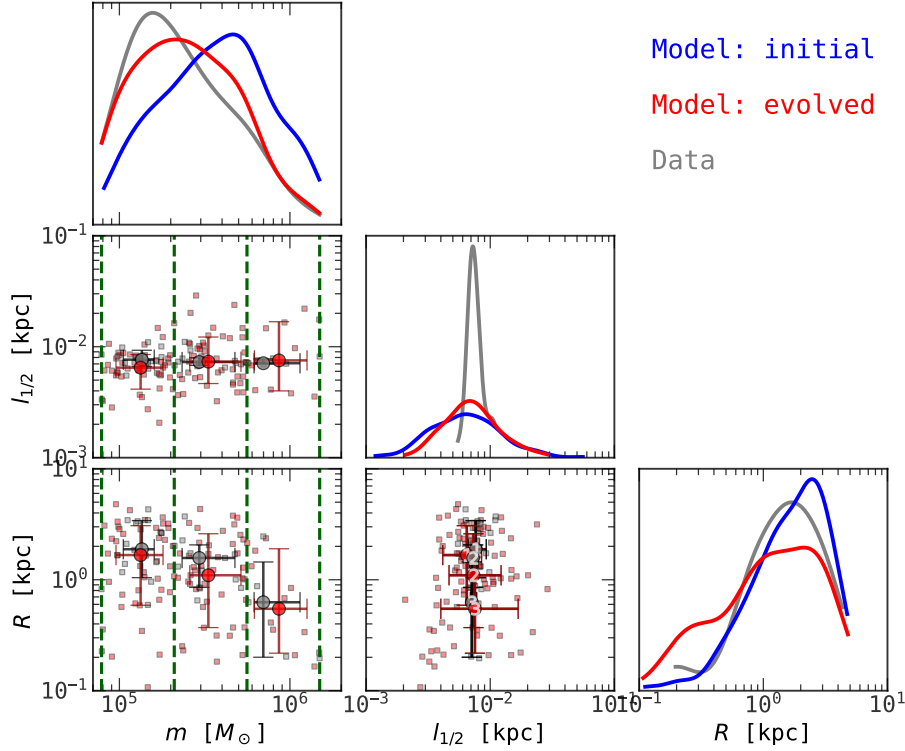


Figure 7. The same as Fig. 5, but for the best-fit Burkert halo.

adopted a simpler model and ignored the details of GC evolution. The most obvious difference that the different profile shapes can cause is actually the fraction of GCs that reach the center of the host galaxy and form a nuclear star cluster. We will discuss this further in Section 4.

3.3. Comparison with scaling relations

With the aforementioned halo-profile constraints, we can see that UDG1 is an outlier in several scaling relations of galaxy-halo connection and halo structure.

First, for normal galaxies, the abundance of GCs, N_{GC} , is an excellent tracer of their host system’s virial mass (Harris et al. 2017): a simple linear relation, $M_{\text{vir}} = 5 \times 10^9 M_\odot \times N_{\text{GC}}$, fits the observational median for almost 5 decades in halo mass from $M_{\text{vir}} \sim 10^{10} M_\odot$ to $10^{15} M_\odot$. The scatter of this relation increases towards the lower-mass end, $\sigma_{\log N_{\text{GC}}} \propto M_{\text{vir}}^{-1/2}$, and is approximately 0.31 dex at $M_{\text{vir}} = 10^{11} M_\odot$ (Burkert & Forbes 2020). The inverse of this relation has been widely used as a halo-mass estimator (e.g., Forbes et al. 2021) and was the basis of the hypothesis that some of the most GC-abundant UDGs are failed L^* galaxies (e.g., van Dokkum et al. 2016). If we assume for simplicity that the scatter in virial mass at a fixed GC abundance is the same as that in the GC abundance at fixed mass, i.e., $\sigma_{\log M_{\text{vir}}} = 0.31$ at $N_{\text{GC}} = 20$ and

$\sigma_{\log M_{\text{vir}}} \propto N_{\text{GC}}^{-1/2}$, then a galaxy with 50 GCs is expected to have a virial mass of $\log M_{\text{vir}} = 10.7 \pm 0.2$. Hence, according to our halo-mass estimates, UDG1, with a virial mass (stars + DM halo) of approximately $M_{\text{vir}} \sim 10^{8.7} M_\odot$, is a dramatic outlier to this empirical $N_{\text{GC}}-M_{\text{vir}}$ relation (as extrapolated to the lower mass range) by several σ . We illustrate this in the upper panel of Fig. 8. Here, the grey band actually represents the full width of the distribution of the observational sample compiled by Burkert & Forbes (2020) – despite the increase of the scatter at the low-mass end, UDG1 is still an outlier.

However, the $N_{\text{GC}}-M_{\text{vir}}$ relation is based on massive normal galaxies, so it does not necessarily apply to ultra-diffuse galaxies, and the extrapolation to the low-mass end ($M_{\text{vir}} \gtrsim 10^{10} M_\odot$) is ungrounded. In fact, as Burkert & Forbes (2020) already noticed, in their effort of explaining this relation with halo merger trees, the relation must flatten at $M_{\text{vir}} \gtrsim 10^{10} M_\odot$ or $N_{\text{GC}} \lesssim 100$, which is exactly the regime of GC-rich UDGs. This flattening is supported by the observational sample of dwarf galaxies whose virial masses are individually constrained with gas kinematics Forbes et al. (2018), as represented by the grey band in Fig. 8. Our virial-mass estimate of UDG1 is in line with the flattening of the $N_{\text{GC}}-M_{\text{vir}}$ relation at the low-mass end, and highlights the danger

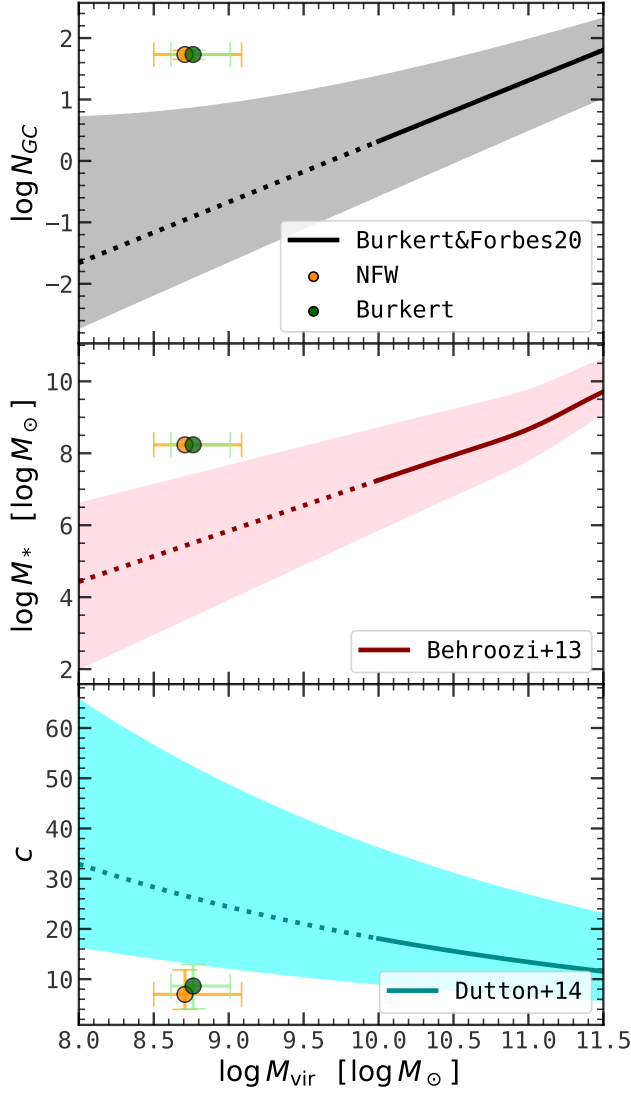


Figure 8. NGC5846-UDG1, with its DM halo constrained with the GC statistics, in comparison with the empirical scaling relations of GC number N_{GC} versus virial mass M_{vir} (*upper*), stellar mass M_* versus virial mass M_{vir} (*middle*), and halo concentration c versus virial mass M_{vir} . The orange/green circles with error bars represent the medians with the 16th and 84th percentiles, assuming NFW/Burkert halo. The lines stand for the median relations from Burkert & Forbes (2020), Behroozi et al. (2013), and Dutton & Macciò (2014), as indicated. The dashed parts of the lines indicate extrapolations to a lower mass range than that of the observational or simulation samples based on which these relations are extracted. The grey band in the upper panel represents the full scatter of the observational sample as in Burkert & Forbes (2020). The red band in the middle panel indicates the 1σ scatter in $\log M_*$ at fixed virial mass, as constrained using dwarf satellites in the ELVES sample, from Danieli et al. (2022a). The cyan band indicates the 1σ scatter of 0.3 dex, assuming log-normal distributions of c at fixed virial masses. UDG1 is an outlier to these scaling laws by $\sim 2-3\sigma$.

of naively inverting the relation to infer virial mass with the number of GCs.

Second, UDG1 is an outlier to the stellar-mass-total-mass relation from abundance matching, as illustrated in the middle panel of Fig. 8. For comparison, we have chosen the median relation as in Behroozi et al. (2013), and recent estimate of the low-mass-end scatter using the dwarf satellites in the ELVES observational sample Danieli et al. (2022a). We caution that despite being intensively studied, the low-mass end of the relation remains highly uncertain, and different assumptions lead to different results (e.g., Danieli et al. 2022a, and the references therein). Our particular choice here is among the most flat for the low-mass-end median slope and among the largest in the scatter – even with these conservative choices, UDG1 is a $\sim 2\sigma$ outlier.

Third, as the bottom panel of Fig. 8 shows, UDG1 stands out with respect to the concentration-mass relation of DM halos. For comparison, we have shown a median c - M_{vir} relation from cosmological N -body simulations (Dutton & Macciò 2014), and a constant scatter of 0.3 dex assuming log-normal c distribution at fixed M_{vir} (Diemer & Kravtsov 2015; Benson 2020).⁵ Obviously, the UDG1 halo is less concentrated than what is expected cosmologically for its mass. This is consistent with the scenario that UDG formation is the consequence of repeated supernovae feedback, which makes both the halo cored and less concentrated but also makes the stellar distribution puffy (e.g., Jiang et al. 2019; Freundlich et al. 2020).

In short, the UDG1 DM halo stands out as a $\sim 2-3\sigma$ outlier compared to all the aforementioned scaling relations, irrespective of the assumed density-profile shape. It is in line with the understanding that there is huge scatter in these relations at the low-mass end, and warns us against generalizing these relations to extreme galaxies and using them as virial mass estimators. We caution that our halo mass estimates for UDG1 is based on the assumption of a static host halo, whereas in reality the UDG1 halo might be a satellite of the galaxy group NGC5846, thus have been environmentally processed and may also have internally-driven evolution due to SNe for example. To consider the host halo of UDG1 as a subhalo evolving in mass and structure is beyond the scope of this work, but it is reasonable to speculate, because of subhalo mass loss, that the peak virial mass of the system in the past (M_{peak}) is higher than our es-

⁵ The scatter in principle varies with mass and the selection of halos based on whether they are relaxed, and 0.3 dex is a ballpark estimate.

timates here, and thus brings the system closer to the empirical scaling laws.

4. DISCUSSION

In this section, we first discuss a few observational implications, including the predictions of the line-of-sight (LOS) velocity dispersion of the GCs in UDG1, and the fraction of nuclear star clusters. Second, we compare our model with that of the previous work of Bar et al. (2022), and combine their model with the MCMC inference as a robustness test of our results on the halo mass and concentration. Finally, we comment on the simplifications in this work, and point out potential future improvements and applications of our method.

4.1. Velocity dispersion of the GCs

In Fig. 9, we present the line-of-sight (LOS) velocity-dispersion profile of the evolved GCs in halos of the best-fit parameters. To make the curve smoother, we have used a thousand GCs. The dispersion profiles in a Burkert halo or in an NFW halo are very similar, and in comparison with the initial dispersion profiles, which reflect the equilibrium kinematics of the host potential, both show a significant decrease at smaller R . This is another manifestation of DF, besides mass segregation. Observationally, Müller et al. (2020) have measured the velocities of 11 of the member GCs of UDG1, and inferred a dispersion of $\sigma = 9.4_{-5.4}^{+7.0}$ km/s at $R \approx 1.8$ kpc (i.e., the average distance of the 11 GCs to the galaxy center), assuming a simple pressure-supported spherical system. Our model predictions agree with this measurement, as shown in Fig. 9. In fact, a closer look at the posterior distribution of the GC velocity dispersion of Müller et al. (2020) reveals that the mode value is approximately 8 km/s, almost exactly on top of our model prediction.

Interestingly, Forbes et al. (2021) measured the velocities of the smooth stellar distribution of UDG1 using KCWI on the Keck telescope, and found a rather high value of the smooth-star velocity dispersion of $\sigma_* = 17 \pm 2$ km/s, higher than the equilibrium value ($\sigma \sim 11$ km/s) of a low-mass ($M_{\text{vir}} \sim 10^9 M_\odot$) system as advocated here, and more consistent with a virial mass of $M_{\text{vir}} \sim 10^{9.5} M_\odot$. We opt not to dive into the factors that may reconcile the tension, such as oversimplifications in our model or non-equilibrium of the stellar distribution. Instead, we can see that these two observational studies together (Müller et al. 2020; Forbes et al. 2021) present a qualitatively similar picture as what our model reveals here, i.e., the GC population of UDG1 have smaller velocity dispersion than the smooth stars,

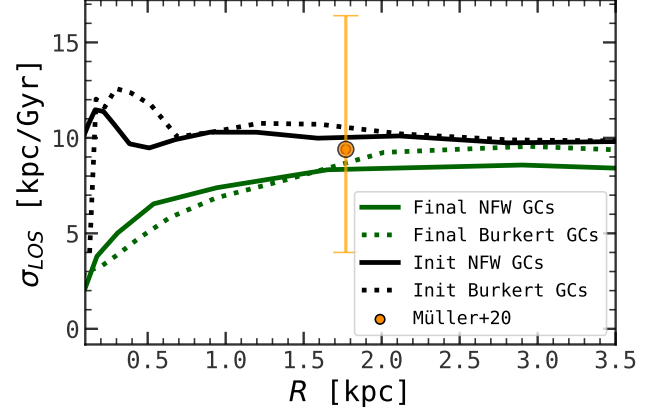


Figure 9. Line-of-sight velocity-dispersion profiles of the star clusters – the initial clusters in the best-fit NFW halo (black solid line), the initial clusters in the best-fit Burkert halo (black dotted line), the evolved GCs in the best-fit NFW halo (green solid line), the evolved GCs in the best-fit Burkert halo (green dotted line). For comparison, the orange circle with error bar is inferred from the kinematics observations (Müller et al. 2020), using about one fifth of all the ~ 50 member GCs. The model predictions is in decent agreement with the observational inference (see Section 4.1).

indicative of DF, and the virial mass of UDG1 is lower than what is expected from the scaling laws.

4.2. Nucleated ultra-diffuse galaxies

A significant fraction of UDGs are nucleated, in the sense that they feature a compact stellar distribution at or near the geometric center of the system (Lim et al. 2018; Greco et al. 2018; Iodice et al. 2020; Marleau et al. 2021). The compact stellar source, also known as the nuclear star cluster, is more compact than a stellar bulge as in an early-type galaxy and is more massive than a typical GC – imaging samples can be found at Lim et al. (2018, Fig.3). The fraction of UDGs that are nucleated is approximately 30-40% in nearby galaxy clusters, and seem to show an environment dependence such that the fraction is higher in the densest region and decreases towards the outskirts of the galaxy cluster (Lim et al. 2018).

It is natural to attribute the formation of the nuclear star clusters to the coalescence of the GCs which have lost their orbital angular momentum completely due to DF and sunk to the center. If this is the case, we can expect that different DM-halo density profiles, as well as different initial GC distributions, can determine the nucleatedness of a UDG and the mass of the nuclear star cluster. Here we explore this scenario using our model. We emphasize that this experiment is a for GC-rich UDGs in general, no longer aimed at reproducing UDG1, but we keep the setup the same for

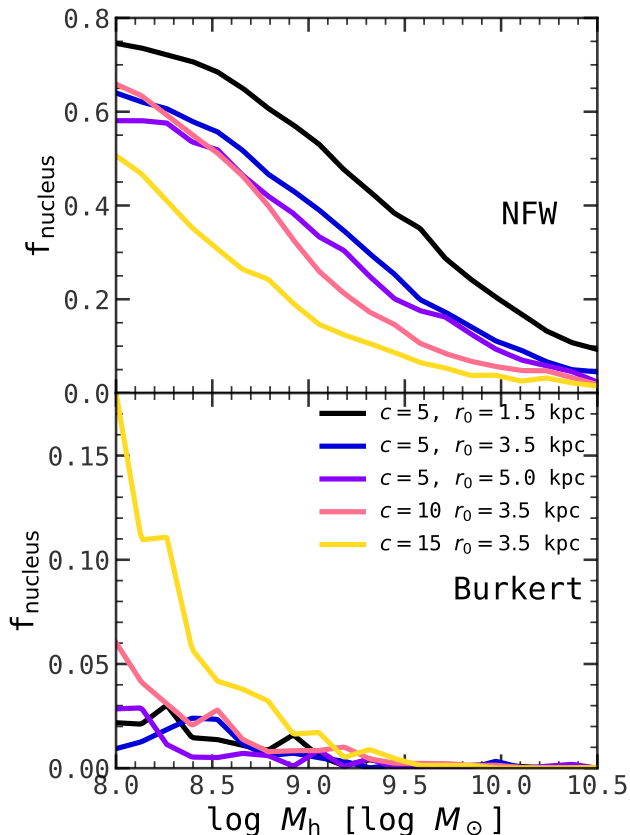


Figure 10. The mass fraction of nuclear star cluster (the total mass of the GCs that have sunk to the center of the galaxy due to dynamical friction, divided by the total mass of all the GCs in the galaxy) as a function of halo mass. The upper and lower panels show the results assuming cuspy (NFW) and cored (Burkert) profiles, respectively. Different colors represent different combinations of the halo concentrations (c) and the scale length (r_0) of the initial GC distribution, as indicated. Clearly, a cuspy, low-mass halo easily gives rise to nucleated systems, while the cored profile yields negligible nuclear star cluster for most parameter combinations.

simplicity. We quantify the nucleatedness of the resulting system using the mass fraction of the nuclear star cluster, f_{nucleus} , defined as the total mass of the GCs that settle to $r < 0.1$ kpc, divided by the total mass of all the GCs.

In Figure 10 we show f_{nucleus} as a function of halo mass M_h , halo concentration c , and the initial Hernquist scale of the GC distribution r_0 . Again, to make the curves smoother, we have used a thousand GCs for each model realization. Here, a cuspy NFW profile and a cored Burkert profile exhibit a dramatic difference, in the sense that the nucleus fraction in a cored halo is almost zero (except for the combination of the lowest M_h , highest c , and largest r_0), whereas that of a cuspy

halo is significant, as long as the halo mass is below $M_h \sim 10^{10} M_\odot$. The negligible nucleus fractions of a cored halo is due to the stalling effect, or the dynamical buoyancy within the core region, which prevents the GCs from dropping deeper, or, if the GCs start out within the core, drives them outwards.

There are trends of the nucleus fraction with the model parameters. First, larger halo mass leads to smaller f_{nucleus} . This is because of the anti-correlation of the strength of DF with the mass ratio between the GC and the host. Second and intuitively, larger scale length leads to smaller f_{nucleus} (although it is not as clear in the Burkert cases, where GCs rarely sink completely anyways), since if GCs start out at large distances, they need stronger DF or longer time to sink to the center. Third, as to the concentration dependence, for NFW halos, a higher concentration leads to a lower f_{nucleus} , at fixed halo mass. This, again, can be attributed to the competing effects on DF from increasing c and increasing M_h , as we discussed in the context of the c - M_h degeneracy of a cuspy halo in Section 3.1. For Burkert halos, the c -trend is vague, and can similarly be attributed to the null effect of varying c on the DF acceleration as we argued in Section 3.2. The difference in the nucleus fraction between the cuspy and cored cases implies the possibility of using nuclear star clusters to infer the DM distribution of UDGs (see e.g., Modak et al. 2022), and could be further explored in future statistical studies.

4.3. Comparison with Bar et al.

We note that Bar et al. (2022) also studied the mass segregation of GCs in UDG1 using a semi-analytical model of dynamical friction of similar nature to ours. There are a couple of major improvements here in our approach.

First, Bar et al. (2022) did not trace the mass and structural evolution of GCs along the orbits, but instead adopted a simple empirical model for GC mass loss, $m(t) = m(0)(1 - \delta t/t_0)$ with $\delta = 0.3$, $t_0 = 10$ Gyr, for all the GCs. That is, the mass evolution is linear with time, irrespective of the local tidal field, and there is no structural evolution. Related, the GC mass distribution in that work was essentially manually set to match that observed. As discussed in Section 2, the mass and structural evolution enter the dynamical-friction treatment, via the Coulomb logarithm, and thus the orbit evolution could be different if the mass or size is not properly accounted for (Fig. 2). In our model, the GCs evolve self-consistently, starting from theoretically-motivated or observationally-motivated initial mass functions and structural distributions and letting tidal effects and two-

body relaxation operate on the GCs. As such, besides the GC mass segregation signal, the evolved GC mass function and size-mass relation are also emergent predictions, and, as demonstrated, they both agree decently with the data.

Second, Bar et al. did not aim at constraining the DM halo mass or structure using the mass segregation signal. Instead, they adopted a couple of fixed halo masses and profiles and tested whether the radial mass segregation could be achieved with DF under these somewhat arbitrary configurations. Specifically, they used an NFW host with $M_h = 10^{9.78} M_\odot$ and $c = 6$, a Burkert host with $M_h = 10^{9.53} M_\odot$ and $c = 15.4$, as well as a pure-stellar potential that matches the observed galaxy. These are single-component host potentials, namely, for the NFW and Burkert hosts, there is no explicit smooth stellar component, and for the pure-stellar case there is no DM halo. Their NFW and Burkert choices are marked as blue crosses in Fig. 4 and Fig. 6. Basically, their halo masses are approximately an order of magnitude higher than what we found in this study, and their halo concentrations happen to be close to our posterior mode values. Hence, not surprisingly and in qualitative agreement with what we found here, the Bar et al. experiment with the NFW host produced a GC distance-mass relation that is shallower than observed, while both their Burkert host and the DM-less cases rendered sufficiently steep mass segregation (see Fig.5 therein).⁶

As a robustness test, we also run model realizations with the Bar et al. mass-loss recipe⁷. We find that for NFW profiles, the mode values are $M_h = 10^{8.78} M_\odot$, $c = 4.24$, $r_0 = 4.48 \text{ kpc}$ and the median values with the 16th and 84th percentiles are $\log(M_h/M_\odot) = 8.64^{+0.45}_{-0.34}$, $c = 8.27^{+4.54}_{-4.01}$, $r_0 = 2.94^{+1.35}_{-1.44} \text{ kpc}$; whereas for Burkert profiles, the mode values are $M_h = 10^{9.95} M_\odot$, $c = 11.04$, $r_0 = 0.12 \text{ kpc}$ and the median values with the 16th and 84th percentiles are $\log(M_h/M_\odot) = 9.50^{+0.26}_{-0.25}$, $c = 9.95^{+3.55}_{-4.45}$, $r_0 = 2.50^{+1.74}_{-1.61} \text{ kpc}$. Compared to the values reported in Section 3 with our fiducial GC evolution model, these results are qualitatively similar, in the sense that they also indicate DM deficiency and a lower-than-normal halo concentration. The halo masses are systematically higher though from the Bar et al. recipe, especially with the assumption of a Burkert halo. This highlights the impact of the details in the GC-evolution

recipe in this kind of models. We discuss this in more detail in Appendix C.

4.4. Simplifications and future work

While in this study we have improved upon a previous study by introducing a self-consistent physical model of GC evolution and employing MCMC to constraint the DM halo properties, we caution that there are still a few simplifications that leave room for future improvements. Addressing them quantitatively is beyond the scope of current work, but here we point out qualitatively how they might affect the results and sketch ideas for future studies. The discussion applies not just to the specific galaxy NGC5846-UDG1, but to GC-rich low-surface-brightness galaxies in general.

First, we have assumed that the host potential is static over the entire evolution of the GC population. However, UDG1 is a satellite galaxy of the galaxy group NGC5846, and many GC-rich low-surface-brightness galaxies are members of galaxy groups or clusters. That is, the host halo of UDG1 may be a subhalo that has experienced significant mass loss if it had reached orbital pericenters sufficiently close to the center of the host group. If this is the case, UDG1 may lie closer to the scaling relations (Section 3.3) if its peak virial mass and the concentration at the peak mass are used in place of the present-day values. In fact, it has been argued that the differential tidal mass loss between the subhalo and the stellar component can produce DM-deficient dwarf galaxies (Moreno et al. 2022). Even for a distinct dwarf galaxy, the host halo is not static, but increases in mass gradually. It is in principle possible to parameterize the mass assembly history of the host halo or subhalo using empirical models extracted from cosmological simulations (e.g., Wechsler et al. 2002). However, this would introduce additional model parameters that need to be marginalized over, not to mention that there is significant halo-to-halo variance in the mass histories (Jiang & Bosch 2017) so that a certain choice of the mass history may not necessarily be representative. A more viable way of exploring statistically the effect of a dynamic host is to post-process cosmological numerical or semi-analytical simulations: to populate simulated halos with GCs and study the GC statistics. We leave this idea to a future study.

Second, there are a few other mechanisms for GC mass and structural evolution besides tidal interactions and two-body relaxation, including, among others, stellar evolution and gravothermal core-collapse. Lamers et al. (2010) provide an empirical formula for mass loss of GCs due to stellar evolution obtained from collisional N -body simulations. Following their model, GCs lose $\sim 25\%$ of

⁶ They could still achieve sufficiently strong mass segregation by manually modifying the GC mass function.

⁷ There are a few other minor differences between our models, including the treatment of the Coulomb logarithm. Here for a simple robustness test, we opt to stick to our model for everything else, and only test if the simplistic mass-evolution model changes the main conclusion.

their initial mass over 10 Gyr, insensitive to their initial masses. Therefore, this effect can simply be offset by shifting the ICMF. The more complicated effect is the gravothermal core-collapse of GCs, which steps in after when an isothermal core is established due to two-body relaxation. The core contracts since it is dynamically hotter than the outer part and transports energy to the outskirts. This makes the GC profile deviate from the EFF profile assumed in this work (or more generally, the King models), and become cuspy and resistant to tidal mass loss. The core-collapse timescale has been estimated to be 12-19 times the relaxation time τ_r given in eq. (14) (Quinlan 1996), so it can be shorter than the Hubble time for the lower mass GCs ($m \lesssim 10^{4.5} M_\odot$).

Third, if future kinematics observations can narrow down the DM profile, we can then adapt our model to constrain the other model ingredients. For instance, while the ICMF is believed to have the functional form of eq. (20), the power-law slope as well as the truncation mass scales are not fully constrained and likely exhibit variation from one population to another (see e.g., Alexander & Gieles 2013, for a discussion on the power-law slope). It would be interesting to treat these three parameters as free parameters, and combine the GC evolution model and the MCMC method as in this study to constrain the ICMF. It would be interesting to investigate, e.g., whether UDGs have a unique ICMF.

5. CONCLUSION

In this work, we are motivated by a remarkable ultra-diffuse galaxy, NGC5846-UDG1, whose GC population exhibits interesting radial mass segregation, and aim to explore the possibility of reproducing the mass segregation of the GCs with DF and constraining the DM content of the UDG using photometric data alone. To this end, we have introduced a simple semi-analytical model that describes the evolution of GC populations in their host DM halo and galaxy, accounting for the effects of DF, tidal evolution, and two-body relaxation. We also consider educated assumptions of the initial properties of the GC progenitors, including the mass function, structure, and spatial distributions. We forward model the GCs in a UDG1-like host potential (consisting of a DM halo and a smooth stellar distribution) to match the observed GC statistics from Danieli et al. (2022b), and use MCMC to constrain the DM-halo properties (halo mass M_h and concentration c) of UDG1, as well as the scale radius of the initial star-cluster spatial distribution (r_0). While we have focused on UDG1, the methodology developed here is generally applicable to low-surface-brightness galaxies with a rich GC popula-

tion. We summarize our methodology and the main findings as follows.

We have shown that the orbital evolution under the influence of DF depends on the mass and structural evolution. Our model can self-consistently evolve the mass and structure of individual GCs along their orbits, capturing the effect of a varying tidal field along an eccentric orbit around the central region of a galaxy. In the limit of a weak tidal field, the mass and structural evolution in our model reduces to that of the classical work of H  non (1965); while in the limit when the timescale for tidal stripping is shorter than two-body relaxation, the structural evolution follows that of the empirical tidal evolution track for collisionless systems of Pe  arrubia et al. (2010) with cored density profiles, which applies to the assumed EFF density profiles of the GCs. Reassuringly, over the timescale of ~ 10 Gyr, a population of star clusters drawn from reasonable initial cluster mass functions (Trujillo-Gomez et al. 2019, ICMF) and initial structure-mass distributions (Brown & Gnedin 2021) evolves in a qualitatively converging manner regarding its evolved mass and size distributions. Notably, the lower-mass clusters ($m \lesssim 10^4 M_\odot$) expand and get dissolved more easily, whereas the most massive clusters ($m \gtrsim 10^6 M_\odot$) remain largely intact, making the evolved GC mass function peak at $m \sim 10^5 M_\odot$ and the evolved GC size-mass relation flat, as observed.

No matter whether the density profile of UDG1 is cuspy or cored, we find that the DM halos that can give rise to the observed mass segregation are with low mass and low concentration. In particular, with an NFW (Burkert) halo, we obtained a posterior-mode halo mass of $M_h = 10^{8.66} M_\odot$ ($10^{8.64} M_\odot$) and concentration of $c = 5.24$ ($c = 11.90$). There is a concentration-mass degeneracy (anti-correlation) in the case of an NFW profile, driven by the competing effects of increasing c and increasing M_h on the DF strength in the central few kpc of the host potential. Given the stellar mass of UDG1 of $M_\star \sim 10^8 M_\odot$, these halo-mass estimates put UDG1 in the dark-matter deficient territory.

In fact, UDG1 is a dramatic outlier compared to both the stellar-to-total-mass relation (e.g., Behroozi et al. 2013; Danieli et al. 2022a) and the GC-abundance-total-mass relation (e.g., Harris et al. 2017; Burkert & Forbes 2020). The latter relation is known to flatten and increase in scatter at the low-mass end, and UDG1, with our halo-mass estimates, is in qualitative agreement with this trend (though more extreme). This warns against using this relation blindly for halo-mass estimates for UDGs.

The estimated halo concentration are lower than the cosmological average value expected for halos of the pos-

terior masses. This lends support to the theoretical picture that UDGs populate low-concentration halos, which are puffed up by repeated supernovae outflows or environmental effects (e.g., Di Cintio et al. 2017; Chan 2019; Jiang et al. 2019). The posterior scale distance of the initial star-cluster distribution (which is assumed to follow an Hernquist profile) is $r_0 = 3.11$ kpc and 3.53 kpc for NFW and Burkert host, respectively. Hence, the star clusters, although currently more concentrated than the smooth stellar distribution of the galaxy, were likely in a more extended configuration initially than the (present-day) smooth stars which has an effective radius of 2 kpc. This may imply that the star clusters are of *ex-situ* origin, but given the oversimplifications we have made regarding the history of the system and the fact that the GCs seem to have a single age, we opt to not make stronger statement in this regard.

The radial mass segregation of GCs can be well reproduced with either assumption of the halo profile. If we focus on the distance-mass slope, i.e., focus on the GCs that have not sunk to the center of the galaxy (Section 3), cuspy and cored halo profiles result in very similar steepness of mass segregation. However, if we include all the GCs including the ones that have completely lost orbital angular momentum due to DF, and consider the nuclear star cluster that form out of GC mergers at the center of the galaxy, then the cuspy NFW halo can yield massive nuclear star clusters provided that the halo mass is below $10^{10} M_\odot$, whereas cored halos do not result in any significant nuclear star cluster. Therefore, a viable formation mechanism for nucleated UDGs (e.g. Lim et al. 2018) is the orbital decay of GCs in a low-mass cuspy halo (see also Modak et al. 2022). As UDG1 seems to be a non-nucleated UDG, we conclude that it is

very likely hosted by an cored, low-mass DM halo. This is, again, in line with the theoretical picture that UDG formation goes hand-in-hand with the core transformation of DM halos due to non-adiabatic perturbations of the gravitational potential.

Last but not the least, compared to the observationally-costly kinematics measurements, our model can reproduce the observed line-of-sight velocity dispersion of the GCs (Müller et al. 2020), and can reveal the difference between the velocity dispersion of the GCs and the background, which also manifests DF and is in qualitative agreement with what is observed (Forbes et al. 2021).

In summary, we have demonstrated with the case study of UDG1 that, as long as low-surface-brightness galaxies host a statistically significant number of GCs and the GCs form a radial mass trend, one can use a computationally efficient semi-analytical model such as the one laid out in this work to constrain the hosting DM distributions. This is feasible with the easily-achievable imaging data alone.

- 1 FJ thank Avishai Dekel, Aaron Romanowski, Frank van
- 2 den Bosch, Hui Li, Kyle Kremer, Xiaolong Du, Ethan
- 3 Nadler, Jacob Shen, and Manoj Kaplinghat for help-
- 4 ful general discussions. JL acknowledges the Tsinghua
- 5 Astrophysics High-Performance Computing platform at
- 6 Tsinghua University for providing computational and
- 7 data storage resources that have contributed to the re-
- 8 search results reported within this paper.

Software: EMCEE (Foreman-Mackey et al. 2013), SatGen (Jiang et al. 2019)

APPENDIX

A. ANALYTICS OF STELLAR PROFILES AND DM HALO PROFILES

This section presents useful analytical expressions for the profiles we use in this work, including NFW (Navarro et al. 1997), Burkert (Burkert 1995), and a profile that describes the stellar density of NGC5846-UDG1. The density profiles are already given in the main text, here we list the enclosed mass (M), gravitational potential (Φ), gravitational acceleration in the cylindrical coordinate system (f_R , $f_\phi = 0$, f_z), and the one-dimensional velocity dispersion (σ) for an isotropic velocity distribution are presented.

A.1. NFW

$$M(r) = M_h \frac{f(x)}{f(c)}, \quad (\text{A1})$$

where $x = r/r_s$ and $f(x) = \ln(1+x) - x/(1+x)$.

$$\Phi(r) = \Phi_0 \frac{\ln(1+x)}{x}, \quad (\text{A2})$$

where $\Phi_0 = -4\pi G \rho_0 r_s^2$

$$f_R = -\frac{\partial \Phi}{\partial R} = \Phi_0 \frac{f(x)}{x} \frac{R}{r^2}, \quad f_z = -\frac{\partial \Phi}{\partial z} = \Phi_0 \frac{f(x)}{x} \frac{z}{r^2},$$

(A3)

where $r = \sqrt{R^2 + z^2}$.

$$\begin{aligned} \sigma^2(r) &= -\Phi_0 x (1+x)^2 \int_x^\infty \frac{f(x')}{x'^3 (1+x')^2} dx' \\ &\approx V_{\max}^2 \left(\frac{1.439x^{0.354}}{1 + 1.176x^{0.725}} \right)^2 \end{aligned} \quad (\text{A4})$$

where the second line is an approximation accurate to 1% for $x = 0.01$ -100 (Zentner & Bullock 2003).

A.2. Burkert

$$M(r) = 2\pi\rho_0 r_s^3 g(x), \quad (\text{A5})$$

where $\rho_0 = M_h / [2\pi r_{\text{vir}}^3 g(c)c^3]$, $g(x) = 0.5 \ln(1+x^2) + \ln(1+x) - \arctan x$, and $x = r/r_s$.

$$\begin{aligned} \Phi(r) &= \frac{\Phi_0}{4x} \left\{ 2(1+x) \left[\arctan \frac{1}{x} + \ln(1+x) \right] \right. \\ &\quad \left. + (1-x) \ln(1+x^2) - \pi \right\}, \end{aligned} \quad (\text{A6})$$

where $\Phi_0 = -4\pi G \rho_0 r_s^2$.

$$f_R = -\frac{\partial \Phi}{\partial R} = \Phi_0 \frac{f_0}{x^2} \frac{R}{r_s}, \quad f_z = -\frac{\partial \Phi}{\partial z} = \Phi_0 \frac{f_0}{x^2} \frac{z}{r_s}, \quad (\text{A7})$$

where $r = \sqrt{R^2 + z^2}$ and $f_0 = 2 \arctan \frac{1}{x} + 2f(x) + 2 \arctan x - \pi$.

$$\begin{aligned} \sigma^2(r) &= -\frac{\Phi_0}{2} (1+x) (1+x^2) \int_x^\infty \frac{f(x')}{x'^2 (1+x') (1+x'^2)} dx' \\ &\approx V_{\max}^{0.299} \frac{e^{x^{0.17}}}{1 + 0.286x^{0.797}}. \end{aligned} \quad (\text{A8})$$

A.3. UDG1 stellar profile

$$\begin{aligned} M(r) &= \frac{M_\star}{2(9+2\sqrt{3}\pi)} \left[\sqrt{3}\pi + 18f_3(x) \right. \\ &\quad \left. - 6\sqrt{3}f_2(x) + 9f_3(x) \right], \end{aligned} \quad (\text{A9})$$

where $x = r/r_s$ with r_s a scale radius ($r_s = 2$ kpc); and

$$f_1(x) = \ln \frac{1-x+x^2}{(1+x)^2}, \quad (\text{A10})$$

$$f_2(x) = \arctan \frac{1-2x}{\sqrt{3}}, \quad (\text{A11})$$

$$f_3(x) = \frac{x}{1+x}. \quad (\text{A12})$$

$$\begin{aligned} \Phi(r) &= \frac{\sqrt{3}\Phi_0}{54x} \left[(1+6x)\pi \right. \\ &\quad \left. + 6(2x-1)f_2(x) + 3\sqrt{3}f_1(x) \right], \end{aligned} \quad (\text{A13})$$

where $\Phi_0 = -4\pi G \rho_0 r_s^2$.

$$f_R = -\frac{\partial \Phi}{\partial R} = \frac{\Phi_0 C}{54r^2} \frac{R}{x}, \quad f_z = -\frac{\partial \Phi}{\partial z} = \frac{\Phi_0 C}{54r^2} \frac{z}{x}, \quad (\text{A14})$$

where $C = \sqrt{3}\pi + 18f_3(x) - 6\sqrt{3}f_2(x) + 9f_1(x)$.

$$\begin{aligned} \sigma^2(r) &= -\frac{\Phi_0}{54} (1+x) (1+x^3) \\ &\quad \times \int_x^\infty \frac{\sqrt{3}\pi + 18f_3(x') - 6\sqrt{3}f_2(x') + 9f_3(x')}{x'^2 (1+x')^2 (1-x'+x'^2)} dx' \\ &\approx -\frac{\Phi_0}{54} \frac{1.845e^{x^{0.104}}}{1 + 0.563x^{1.158}} \end{aligned} \quad (\text{A15})$$

where the second line is an approximation specifically for UDG1.

B. GC PROFILE: EFF PROFILE

The EFF profile (Elson et al. 1987) is specified by the total mass, m_{tot} , the scale length a , and the power-law slope η – the density profile is given by

$$\rho(l) = \frac{\rho_0}{(1+l^2/a^2)^\eta}, \quad (\text{B16})$$

where

$$\rho_0 = \frac{\Gamma(\eta)}{\pi^{3/2}\Gamma(\eta-1)} \frac{m_{\text{tot}}}{a^3} \quad (\text{B17})$$

is the central density, with $\Gamma(x)$ the Gamma function.

The enclosed mass of EFF profile is given by

$$m(l) = \frac{4\pi}{3} l^3 \rho_0 \mathcal{F}_{21} \left(\frac{3}{2}, \eta; \frac{5}{2}; -\frac{l^2}{a^2} \right), \quad (\text{B18})$$

where $\mathcal{F}_{21}(a, b; c; z)$ is the hypergeometric function. By solving $m(l) = 0.5m_{\text{tot}}$, one can show that the half-mass radius is given by

$$l_{1/2} = (2^{\frac{2}{2\eta-3}} - 1)^{1/2} a, \quad (\text{B19})$$

a quantity that is repeated used in our model.

As mentioned in Section 2.2, to estimate the tidal heating parameter f_t , we have used the tidal evolution track of Peñarrubia et al. (2010) expressed in terms of the maximum-circular velocity v_{max} and the

radius l_{\max} at which v_{\max} is reached. To this end, we need a relation between l_{\max} and the parameters defining the profile, which is obtained as follows. The radius at which the circular velocity reaches maximum, l_{\max} , is given by the solution of $dv_{\text{circ}}^2/dl = 0$, i.e.,

$$\mathcal{F}_{21}\left(\frac{3}{2}, \eta; \frac{5}{2}; -\frac{l^2}{a^2}\right) - \frac{3\eta}{5} \frac{l^2}{a^2} \mathcal{F}_{21}\left(\frac{5}{2}, \eta + 1; \frac{7}{2}; -\frac{l^2}{a^2}\right) = 0, \quad (\text{B20})$$

and is well approximated by

$$l_{\max} \approx 1.825a \quad (\text{B21})$$

for $\eta = 2$.

C. GC MASS-DISTANCE RELATIONS

As mentioned in Section 2.4, to facilitate parameter inference, we pre-compute the model predictions with one thousand GCs on a mesh grid spanned by the parameters of interest, and perform linear interpolation for model evaluations during the MCMC run.

Using the tabulated results, we plot the median relations between the evolved GC mass and distance for

different halo mass M_h and different scale length r_0 of the initial star-cluster distribution, in Figs. 11-14. The concentrations are kept fixed. Fig. 11 is for NFW halos of $c = 5.24$; Fig. 12 is for Burkert halos of $c = 11.90$. These are the posterior mode values. Fig. 13 is with the Bar et al. (2022) mass-loss recipe and NFW halos of $c = 6$; Fig. 14 is with the Bar et al. mass-loss recipe and Burkert halos of $c = 15$. These values are what Bar et al. adopted.

For the Bar et al. recipe, we assume that the GC sizes are fixed, given by the BG21 relation, since their model does not consider structural evolution. Note that the size information enters the DF calculations, via eq. (5). As can be seen from the last panel of Fig. 13, it is difficult to reproduce the mass segregation using their mass-loss recipe and with their halo parameters for NFW halo. For Burkert halos, we can reproduce mass segregation using their mass-loss recipe and halo mass, at certain scale lengths, as shown in the last panel of Fig. 14. Similar results are reported in their paper.

For our models (Figs. 11-12), one can see clear mass segregation at $M_h \gtrsim 10^9 M_\odot$ and large r_0 .

REFERENCES

- Alexander, P. E. R., & Gieles, M. 2013, MNRAS, 432, L1, doi: [10.1093/mnras/slt022](https://doi.org/10.1093/mnras/slt022)
- Amorisco, N. C., & Loeb, A. 2016, Monthly Notices of the Royal Astronomical Society: Letters, 459, L51, doi: [10.1093/mnras/slw055](https://doi.org/10.1093/mnras/slw055)
- Bar, N., Danieli, S., & Blum, K. 2022, ApJL, 932, L10, doi: [10.3847/2041-8213/ac70df](https://doi.org/10.3847/2041-8213/ac70df)
- Behroozi, P. S., Wechsler, R. H., & Conroy, C. 2013, ApJ, 770, 57, doi: [10.1088/0004-637X/770/1/57](https://doi.org/10.1088/0004-637X/770/1/57)
- Benavides, J. A., Sales, L. V., Abadi, M. G., et al. 2022, arXiv e-prints, arXiv:2209.07539, <https://arxiv.org/abs/2209.07539>
- Benson, A. J. 2020, MNRAS, 493, 1268, doi: [10.1093/mnras/staa341](https://doi.org/10.1093/mnras/staa341)
- Benson, A. J., & Du, X. 2022, MNRAS, 517, 1398, doi: [10.1093/mnras/stac2750](https://doi.org/10.1093/mnras/stac2750)
- Binney, J., & Tremaine, S. 2008, Galactic Dynamics: Second Edition
- Boylan-Kolchin, M., Ma, C., & Quataert, E. 2008, Monthly Notices of the Royal Astronomical Society, 383, 93, doi: [10.1111/j.1365-2966.2007.12530.x](https://doi.org/10.1111/j.1365-2966.2007.12530.x)
- Brown, G., & Gnedin, O. Y. 2021, MNRAS, 508, 5935, doi: [10.1093/mnras/stab2907](https://doi.org/10.1093/mnras/stab2907)
- Burkert, A. 1995, ApJL, 447, L25, doi: [10.1086/309560](https://doi.org/10.1086/309560)
- Burkert, A., & Forbes, D. A. 2020, AJ, 159, 56, doi: [10.3847/1538-3881/ab5b0e](https://doi.org/10.3847/1538-3881/ab5b0e)
- Carleton, T., Errani, R., Cooper, M., et al. 2019, Monthly Notices of the Royal Astronomical Society, 485, 382, doi: [10.1093/mnras/stz383](https://doi.org/10.1093/mnras/stz383)
- Chan, T. K. 2019, PhD thesis, University of California, San Diego
- Chandrasekhar, S. 1943, ApJ, 97, 255, doi: [10.1086/144517](https://doi.org/10.1086/144517)
- Danieli, S., Greene, J. E., Carlsten, S., et al. 2022a, arXiv e-prints, arXiv:2210.14233, <https://arxiv.org/abs/2210.14233>
- Danieli, S., van Dokkum, P., Trujillo-Gomez, S., et al. 2022b, ApJL, 927, L28, doi: [10.3847/2041-8213/ac590a](https://doi.org/10.3847/2041-8213/ac590a)
- Di Cintio, A., Brook, C. B., Dutton, A. A., et al. 2017, MNRAS, 466, L1, doi: [10.1093/mnras/slw210](https://doi.org/10.1093/mnras/slw210)
- Diemer, B., & Kravtsov, A. V. 2015, ApJ, 799, 108, doi: [10.1088/0004-637X/799/1/108](https://doi.org/10.1088/0004-637X/799/1/108)
- Dutta Chowdhury, D., van den Bosch, F. C., & van Dokkum, P. 2020, ApJ, 903, 149, doi: [10.3847/1538-4357/abb947](https://doi.org/10.3847/1538-4357/abb947)
- Dutton, A. A., & Macciò, A. V. 2014, MNRAS, 441, 3359, doi: [10.1093/mnras/stu742](https://doi.org/10.1093/mnras/stu742)
- Elson, R. A. W., Fall, S. M., & Freeman, K. C. 1987, ApJ, 323, 54, doi: [10.1086/165807](https://doi.org/10.1086/165807)

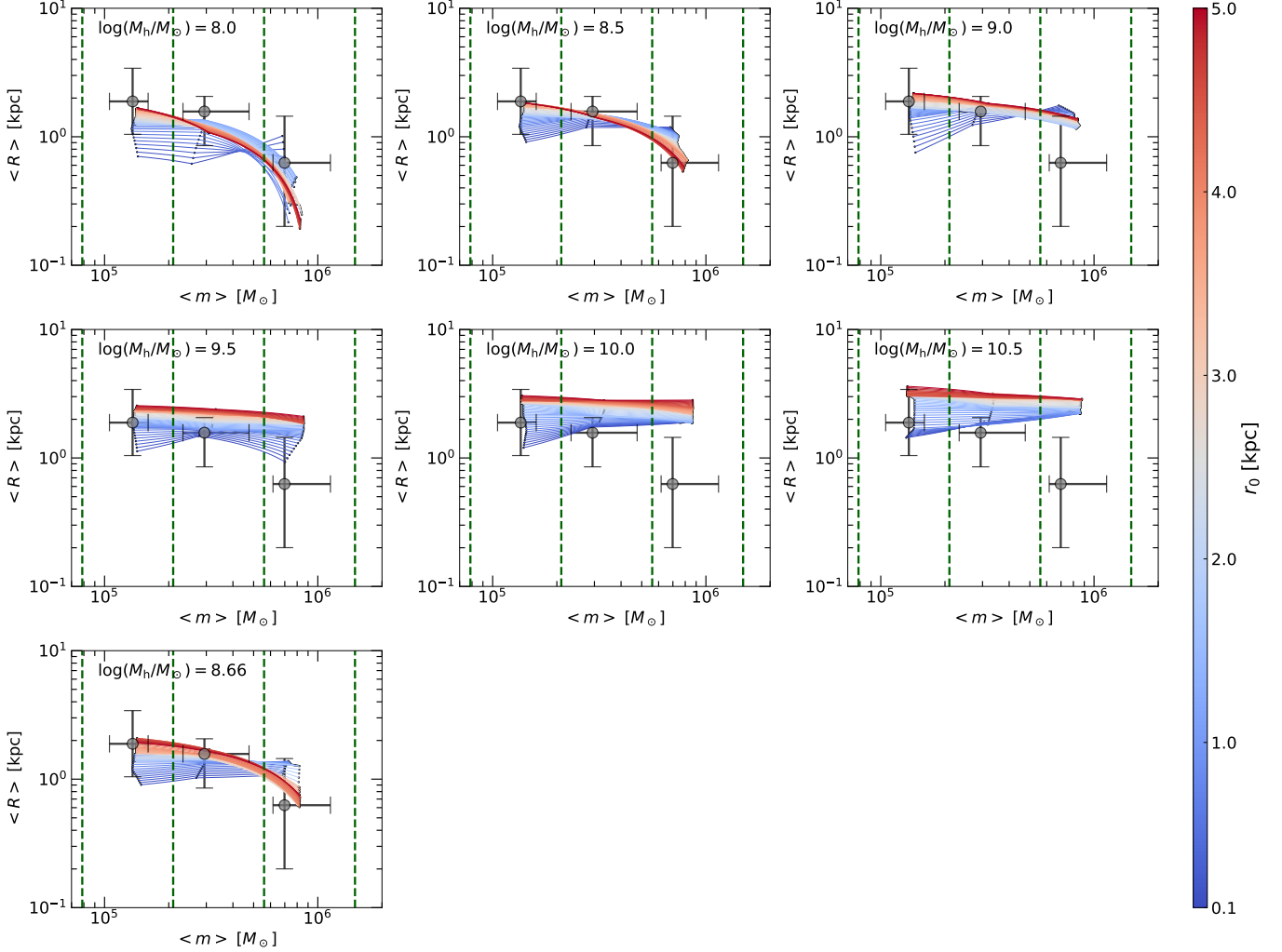


Figure 11. The median galactocentric distance $\langle R \rangle$ versus the median GC mass $\langle m \rangle$, in three mass bins, for different host halo masses (M_h) and different scale distance of the initial star-cluster distribution (r_0). The green dashed lines stand for the boundaries of the mass bins. The gray circles represent the data with the error bars indicating the 16th and 84th percentiles (the same across panels). The lines are model realizations for NFW halos with concentration $c = 5.24$ fixed. The last panel shows the results corresponding to the posterior-mode halo mass.

Forbes, D. A., Gannon, J. S., Romanowsky, A. J., et al. 2021, MNRAS, 500, 1279, doi: [10.1093/mnras/staa3289](https://doi.org/10.1093/mnras/staa3289)
 Forbes, D. A., Read, J. I., Gieles, M., & Collins, M. L. M. 2018, MNRAS, 481, 5592, doi: [10.1093/mnras/sty2584](https://doi.org/10.1093/mnras/sty2584)
 Foreman-Mackey, D., Hogg, D. W., Lang, D., & Goodman, J. 2013, PASP, 125, 306, doi: [10.1086/670067](https://doi.org/10.1086/670067)
 Freundlich, J., Dekel, A., Jiang, F., et al. 2020, MNRAS, 491, 4523, doi: [10.1093/mnras/stz3306](https://doi.org/10.1093/mnras/stz3306)
 Gan, J., Kang, X., van den Bosch, F. C., & Hou, J. 2010, MNRAS, 408, 2201, doi: [10.1111/j.1365-2966.2010.17266.x](https://doi.org/10.1111/j.1365-2966.2010.17266.x)
 Gieles, M., Heggie, D. C., & Zhao, H. 2011, MNRAS, 413, 2509, doi: [10.1111/j.1365-2966.2011.18320.x](https://doi.org/10.1111/j.1365-2966.2011.18320.x)
 Gieles, M., & Renaud, F. 2016, MNRAS, 463, L103, doi: [10.1093/mnras/rlw163](https://doi.org/10.1093/mnras/rlw163)

Goerdt, T., Moore, B., Read, J. I., Stadel, J., & Zemp, M. 2006, MNRAS, 368, 1073, doi: [10.1111/j.1365-2966.2006.10182.x](https://doi.org/10.1111/j.1365-2966.2006.10182.x)
 Greco, J. P., Greene, J. E., Strauss, M. A., et al. 2018, ApJ, 857, 104, doi: [10.3847/1538-4357/aab842](https://doi.org/10.3847/1538-4357/aab842)
 Green, S. B., van den Bosch, F. C., & Jiang, F. 2021, MNRAS, 503, 4075, doi: [10.1093/mnras/stab696](https://doi.org/10.1093/mnras/stab696)
 Guo, Q., Hu, H., Zheng, Z., et al. 2020, Nature Astronomy, 4, 246, doi: [10.1038/s41550-019-0930-9](https://doi.org/10.1038/s41550-019-0930-9)
 Harris, W. E., Blakeslee, J. P., & Harris, G. L. H. 1917, ApJ, 836, 67, doi: [10.3847/1538-4357/836/1/67](https://doi.org/10.3847/1538-4357/836/1/67)
 Harris, W. E., Harris, G. L., & Hudson, M. J. 2015, ApJ, 806, 36, doi: [10.1088/0004-637X/806/1/36](https://doi.org/10.1088/0004-637X/806/1/36)
 Hénon, M. 1965, Annales d'Astrophysique, 28, 992
 Hernquist, L. 1990, ApJ, 356, 359, doi: [10.1086/168845](https://doi.org/10.1086/168845)

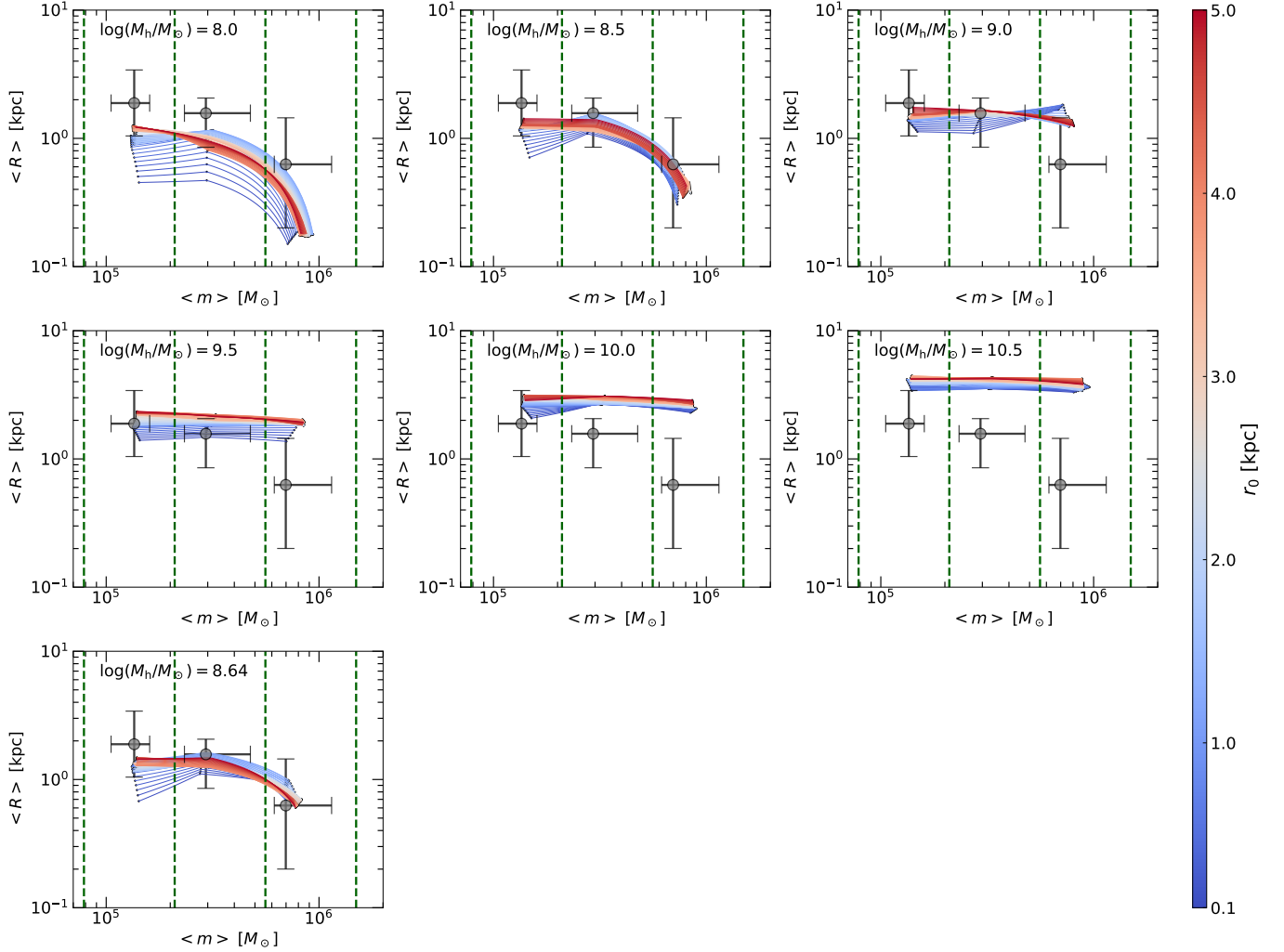


Figure 12. The same as Fig. 11, but for Burkert halos with $c = 11.90$.

Hudson, M. J., Harris, G. L., & Harris, W. E. 2014, *ApJL*, 787, L5, doi: [10.1088/2041-8205/787/1/L5](https://doi.org/10.1088/2041-8205/787/1/L5)

Inoue, S. 2009, *MNRAS*, 397, 709, doi: [10.1111/j.1365-2966.2009.15066.x](https://doi.org/10.1111/j.1365-2966.2009.15066.x)

Iodice, E., Cantiello, M., Hilker, M., et al. 2020, *A&A*, 642, A48, doi: [10.1051/0004-6361/202038523](https://doi.org/10.1051/0004-6361/202038523)

Jiang, F., & Bosch, F. C. v. d. 2017, *Monthly Notices of the Royal Astronomical Society*, 472, 657, doi: [10.1093/mnras/stx1979](https://doi.org/10.1093/mnras/stx1979)

Jiang, F., Dekel, A., Freundlich, J., et al. 2019, *MNRAS*, 487, 5272, doi: [10.1093/mnras/stz1499](https://doi.org/10.1093/mnras/stz1499)

Just, A., Khan, F. M., Berczik, P., Ernst, A., & Spurzem, R. 2011, *MNRAS*, 411, 653, doi: [10.1111/j.1365-2966.2010.17711.x](https://doi.org/10.1111/j.1365-2966.2010.17711.x)

Kaur, K., & Sridhar, S. 2018, *ApJ*, 868, 134, doi: [10.3847/1538-4357/aacbf](https://doi.org/10.3847/1538-4357/aacbf)

King, I. 1962, *AJ*, 67, 471, doi: [10.1086/108756](https://doi.org/10.1086/108756)

Lamers, H. J. G. L. M., Baumgardt, H., & Gieles, M. 2010, *MNRAS*, 409, 305, doi: [10.1111/j.1365-2966.2010.17309.x](https://doi.org/10.1111/j.1365-2966.2010.17309.x)

Liao, S., Gao, L., Frenk, C. S., et al. 2019, *MNRAS*, 490, 5182, doi: [10.1093/mnras/stz2969](https://doi.org/10.1093/mnras/stz2969)

Lim, S., Peng, E. W., Côté, P., et al. 2018, *ApJ*, 862, 82, doi: [10.3847/1538-4357/aacbf81](https://doi.org/10.3847/1538-4357/aacbf81)

Marleau, F. R., Habas, R., Poulain, M., et al. 2021, *A&A*, 654, A105, doi: [10.1051/0004-6361/202141432](https://doi.org/10.1051/0004-6361/202141432)

Modak, S., Danieli, S., & Greene, J. E. 2022, *arXiv*, doi: [10.48550/arxiv.2211.01384](https://doi.org/10.48550/arxiv.2211.01384)

Moreno, J., Danieli, S., Bullock, J. S., et al. 2022, *Nature Astronomy*, 6, 496, doi: [10.1038/s41550-021-01598-4](https://doi.org/10.1038/s41550-021-01598-4)

Müller, O., Marleau, F. R., Duc, P.-A., et al. 2020, *A&A*, 640, A106, doi: [10.1051/0004-6361/202038351](https://doi.org/10.1051/0004-6361/202038351)

Navarro, J. F., Frenk, C. S., & White, S. D. M. 1997, *ApJ*, 490, 493, doi: [10.1086/304888](https://doi.org/10.1086/304888)

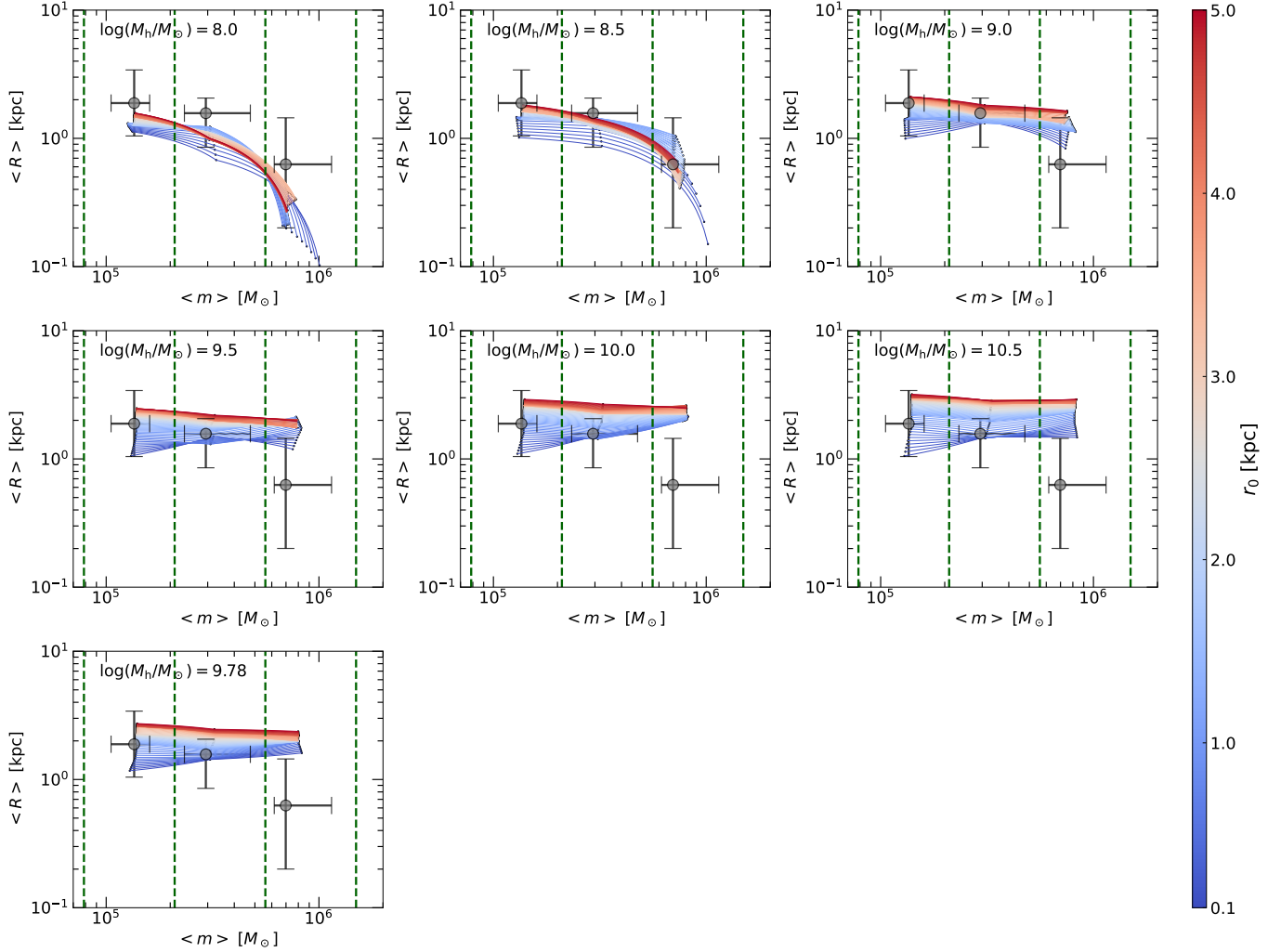


Figure 13. The same as Fig. 11, but with the GC mass-evolution recipe as in Bar et al. (2022), and NFW halos of $c = 6$. The last panel shows the results using the NFW halo mass adopted in Bar et al..

Peñarrubia, J., Benson, A. J., Walker, M. G., et al. 2010, MNRAS, 406, 1290, doi: [10.1111/j.1365-2966.2010.16762.x](https://doi.org/10.1111/j.1365-2966.2010.16762.x)

Petts, J. A., Gualandris, A., & Read, J. I. 2015, MNRAS, 454, 3778, doi: [10.1093/mnras/stv2235](https://doi.org/10.1093/mnras/stv2235)

Petts, J. A., Read, J. I., & Gualandris, A. 2016, MNRAS, 463, 858, doi: [10.1093/mnras/stw2011](https://doi.org/10.1093/mnras/stw2011)

Quinlan, G. D. 1996, NewA, 1, 255, doi: [10.1016/S1384-1076\(96\)00018-8](https://doi.org/10.1016/S1384-1076(96)00018-8)

Read, J. I., Goerdt, T., Moore, B., et al. 2006, MNRAS, 373, 1451, doi: [10.1111/j.1365-2966.2006.11022.x](https://doi.org/10.1111/j.1365-2966.2006.11022.x)

Rong, Y., Guo, Q., Gao, L., et al. 2017, MNRAS, 470, 4231, doi: [10.1093/mnras/stx1440](https://doi.org/10.1093/mnras/stx1440)

Ryon, J. E., Bastian, N., Adamo, A., et al. 2015, Monthly Notices of the Royal Astronomical Society, 452, doi: [10.1093/mnras/stv1282](https://doi.org/10.1093/mnras/stv1282)

Sales, L. V., Navarro, J. F., Peñafiel, L., et al. 2020, MNRAS, 494, 1848, doi: [10.1093/mnras/staa854](https://doi.org/10.1093/mnras/staa854)

Silk, J. 2017, ApJL, 839, L13, doi: [10.3847/2041-8213/aa67da](https://doi.org/10.3847/2041-8213/aa67da)

Spitzer, L. 1987, Dynamical evolution of globular clusters

Sánchez-Janssen, R., Côté, P., Ferrarese, L., et al. 2019, The Astrophysical Journal, 878, 18, doi: [10.3847/1538-4357/aaf4fd](https://doi.org/10.3847/1538-4357/aaf4fd)

Tremmel, M., Wright, A. C., Brooks, A. M., et al. 2020, MNRAS, 497, 2786, doi: [10.1093/mnras/staa2015](https://doi.org/10.1093/mnras/staa2015)

Trujillo-Gomez, S., Reina-Campos, M., & Kruijssen, J. M. D. 2019, MNRAS, 488, 3972, doi: [10.1093/mnras/stz1932](https://doi.org/10.1093/mnras/stz1932)

van Dokkum, P., Danieli, S., Abraham, R., Conroy, C., & Romanowsky, A. J. 2019, ApJL, 874, L5, doi: [10.3847/2041-8213/ab0d92](https://doi.org/10.3847/2041-8213/ab0d92)

van Dokkum, P., Abraham, R., Brodie, J., et al. 2016, ApJL, 828, L6, doi: [10.3847/2041-8205/828/1/L6](https://doi.org/10.3847/2041-8205/828/1/L6)

van Dokkum, P., Abraham, R., Romanowsky, A. J., et al. 2017, ApJL, 844, L11, doi: [10.3847/2041-8213/aa7ca2](https://doi.org/10.3847/2041-8213/aa7ca2)

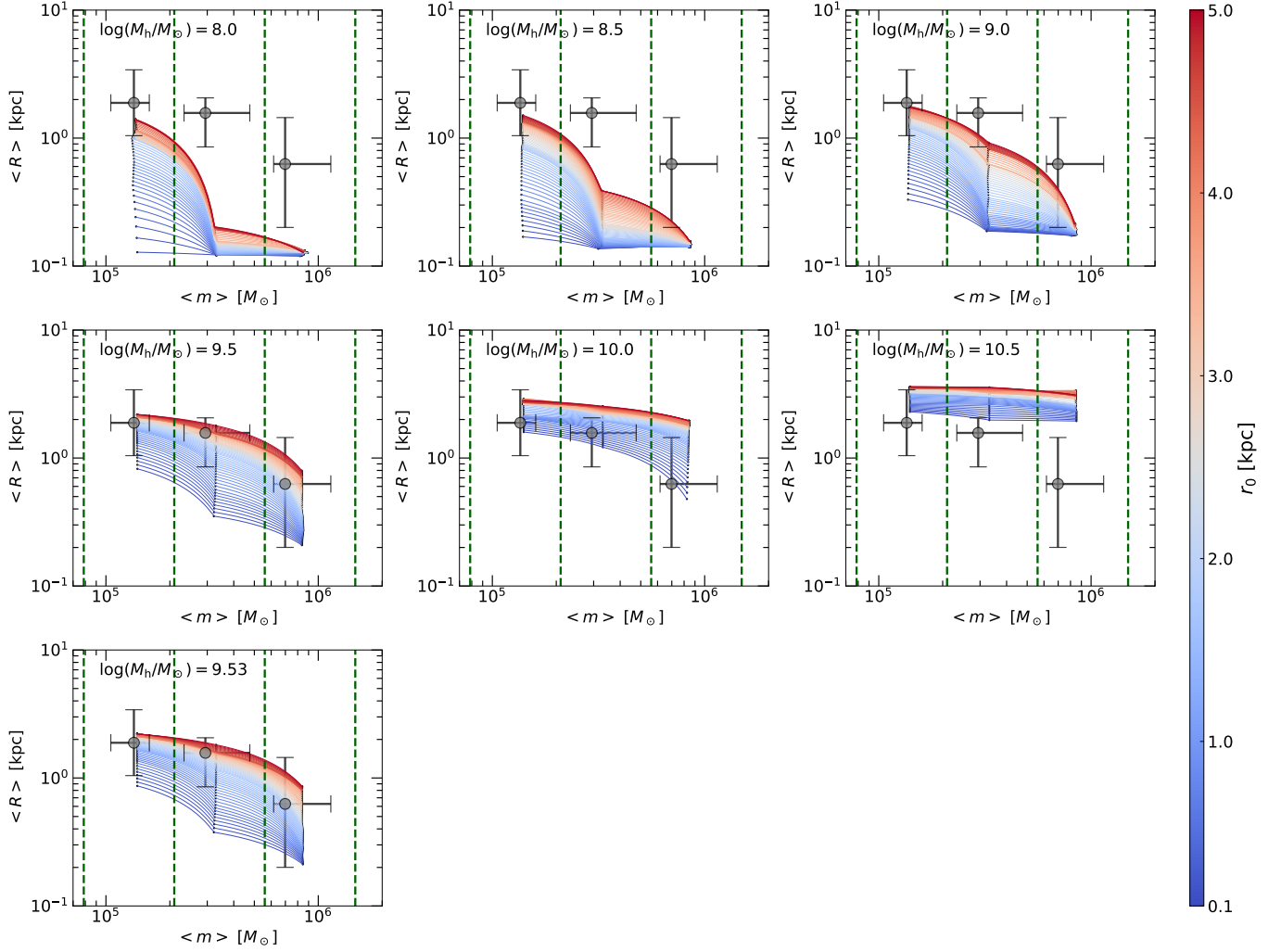


Figure 14. The same as Fig. 11, but with the GC mass-evolution recipe as in Bar et al. (2022), and Burkert halos of $c = 15$. The last panel shows the results using the Burkert halo mass adopted in Bar et al.

van Dokkum, P., Danieli, S., Cohen, Y., et al. 2018, *Nature*,
555, 629, doi: [10.1038/nature25767](https://doi.org/10.1038/nature25767)

van Dokkum, P., Shen, Z., Keim, M. A., et al. 2022,
Nature, 605, 435, doi: [10.1038/s41586-022-04665-6](https://doi.org/10.1038/s41586-022-04665-6)

Wechsler, R. H., Bullock, J. S., Primack, J. R., Kravtsov,
A. V., & Dekel, A. 2002, *ApJ*, 568, 52,
doi: [10.1086/338765](https://doi.org/10.1086/338765)

Zentner, A. R., & Bullock, J. S. 2003, *ApJ*, 598, 49,

doi: [10.1086/378797](https://doi.org/10.1086/378797)